Rock Mech Rock Eng (2012) 45:649–675
DOI 10.1007/s00603-012-0231-4

ORIGINAL PAPER

A Bonded Particle Model Simulation of Shear Strength and Asperity Degradation for Rough Rock Fractures

Mohammad Sadegh Asadi · Vamegh Rasouli · Giovanni Barla

Received: 1 November 2011 / Accepted: 12 February 2012 / Published online: 8 March 2012

Abstract Different failure modes during fracture shearing have been introduced including normal dilation or sliding, asperity cut-off and degradation. Attempts have been made to study these mechanisms using analytical, experimental and numerical methods. However, the majority of the existing models simplify the problem, which leads to unrealistic results. With this in mind, the aim of this paper is to simulate the mechanical behaviour of synthetic and rock fracture profiles during direct shear tests by using the two-dimensional particle flow computer code PFC2D. Correlations between the simulated peak shear strength and the fracture roughness parameter D_{R1} recently proposed by Rasouli and Harrison (2010) are developed. Shear test simulations are carried out with PFC2D and the effects of the geometrical features as well as the model micro-properties on the fracture shear behaviour are studied. The shear strength and asperity degradation processes of synthetic profiles including triangular, sinusoidal and randomly generated profiles are analysed. Different failure modes including asperity sliding, cut-off, and asperity degradation are explicitly observed and compared with the available models. The D_{R1} parameter is applied to the analysis of synthetic and rock fracture profiles. Accordingly, correlations are developed between D_{R1} and the peak shear strength obtained from simulations and by using analytical solutions. The results are shown to be in good agreement with the basic understanding of rock fracture shear behaviour and asperity contact degradation.

Keywords Fracture · Shear strength · PFC · Roughness · Asperity degradation · Simulation · D_{R1}

M. S. Asadi (✉)
Baker Hughes, Perth, WA, Australia
e-mail: sadegh.asadi@bakerhughes.com

V. Rasouli
Curtin University, Perth, WA, Australia

G. Barla
Politecnico di Torino, Torino, Italy

1 Introduction

Fractures in a rock mass control the strength and deformation properties of natural and engineering rock structures. The fracture properties including the basic friction angle, combined with surface roughness, wall compressive strength, presence of infilling material, normal and shear stiffness and water pressure influence the shear strength of the fractured rock mass (Barton 1973; ISRM 1978). Among these parameters, the surface roughness influences not only the peak shear strength of the discontinuity but also the post-peak behaviour, i.e. strain softening.

Fracture roughness increases the shear strength of the rock mass particularly in an underground environment where dilation of the rock along the fracture surface is partially or completely constrained. Under this condition, the stress applied normal to the plane of the fractures increases leading to the closure of open fractures and substantially higher fracture shear strengths. When the applied shear and normal stresses are large, shear failure may take place by both sliding and dilation along the fracture surface. It may also involve tensile fracturing through intact rock fracture asperities as they are sheared off and the shear strength of the fracture falls to a residual value (Asadi and Rasouli 2011; Karami and Stead 2008).

Empirical and mathematical models have been developed to determine the fracture shear strength in relation to the effect of roughness. Since Patton's bilinear model of saw-

tooth joints (Patton 1966), peak shear strength criteria have been developed by Barton and Choubey (1977) and several others and the post-peak response and asperity degradation have been modelled using several experimental, empirical, and theoretical approaches (Asadollahi and Tonon 2010; Bandis et al. 1983; Belem et al. 2000, 2007; Ferrero et al. 2010; Lee et al. 2001; Plesha 1987; Saito et al. 2007).

Constitutive models for joint behaviour consider a large number of assumptions and uncertainties due to the complexity associated with the appropriate characterisation of fracture surface roughness. Despite the large number of papers in the literature presenting different approaches to the roughness assessment problem, the geometric complexity of rock fracture surfaces means that objective assessment and characterisation of roughness remains a challenge. JRC as introduced by Barton and Choubey (1977) is perhaps the most commonly used parameter for fracture roughness. However, using JRC introduces uncertainties in estimating the fracture shear strength, as JRC is a subjective parameter based on the comparison of the rock fracture surface with 10 standard roughness profiles.

The 1D Riemannian parameter D_{R1} which indicates the profile roughness in terms of the magnitude of variation of normal vectors to the profile, has been recently developed by Rasouli and Harrison (2010). Analytical formulae have been proposed by which D_{R1} can be calculated for synthetic profiles of symmetric and asymmetric triangular and sinusoidal geometries. Also, having the (x, y) coordinates of a rock fracture profile, D_{R1} can be estimated numerically. In this paper, an attempt is made to examine the existence of a link between fracture shear strength and D_{R1}.

Numerical studies to investigate the fracture shear behaviour are generally developed based on continuum modelling to predict the onset of failure. However, it is to be noted that the discrete element method (DEM) may enable one to better investigate the failure progression of a fracture surface during shearing by tracking the extent of the damage zone (Jing and Stephansson 2007; Potyondy and Cundall 2004). Cundall (2000) used PFC2D to simulate shear tests on rough fractures and stated that this model is capable to calculate the shear strength of fractures based on correlations with the Barton shear strength criterion (Barton and Choubey 1977) in which roughness is characterised by JRC.

Similarly, Karami and Stead (2008) performed numerical simulations using the FEM/DEM method and examined shear strengths of JRC profiles. They reported on the presence of asperity degradation and development of micro-cracks under high normal stress during fracture shearing. Similarly, Giacomini et al. (2008) performed FEM simulations with the Abaqus code to model the shear strength of synthetic saw-tooth profiles. They also considered the experimental study performed by Yang and Chiang (2000) who used the simple saw-tooth geometry.

Cho et al. (2008) used a DEM code to simulate direct shear tests of fractures. They showed that cracks developed during the test were predominantly tension cracks. These cracks started to grow from the upper edge of the shear box due to the highly non-uniform stress distribution along the shear plane. Most recently, Park and Song (2009) used PFC3D to simulate the fracture direct shear test considering rock fracture micro-properties effects. They also examined JRC profiles shear strength and stressed the effects of particle size, particle friction coefficient and contact bond strength (CBS).

In this paper the shear behaviour of synthetic and rock fracture profiles is simulated with the PFC2D code which is based on DEM, implements the bonded particle model (BPM), and simulates the rock domain using the interaction between an assembly of circular discs (in 2D) (Itasca Consulting Group 2008; Potyondy and Cundall 2004). The ability of PFC2D to simulate the shear strength and asperity degradation of fracture profiles with rough geometries is discussed.

To investigate the mechanical behaviour of the asperities during sliding and degradation, an analytical solution based on the limit equilibrium method and the Mohr–Coulomb failure criterion, similar to that presented by Huang et al. (2002), is also used. This analytical solution is then applied to develop correlations between simulated peak shear strengths and calculated D_{R1} for a variety of fracture profiles.

Finally, the shear strength of synthetic and rock fracture profiles is simulated using PFC2D. The results show that in general as D_{R1} increases the shear strength increases. Asperity degradations are also observed for fracture profiles with large D_{R1} at high normal stress. The results are analysed and for these specific fracture profiles correlations between D_{R1} and peak shear strength are developed. Although the applicability of this correlation may be limited at this stage, D_{R1} is shown to be a representative parameter to characterise the roughness profile and to estimate the shear strength of rock fractures.

2 Bonded Particle Model (BPM)

Rock behaves like a cemented granular material with complex-shaped grains in which both the grains and the cement are deformable (Potyondy and Cundall 2004). Various numerical models have been proposed that mimic such a system. The DEM based model for granular materials, the so-called bonded particle model (BPM), is capable to simulate rock behaviour. This is governed by the development, extent and interaction of micro-cracks, which can be progressively modelled using BPM.

It is also possible to create particles of arbitrary shape by attaching several particles together that create a cluster of particles (Itasca Consulting Group 2008). It has been shown that the clumped particle model (CPM) can better represent the stress–strain behaviour of intact rock in which clusters of disc-shaped particles are defined as rock grains (Cho et al. 2007).

PFC2D (Itasca Consulting Group 2008) is a commercial code based on DEM in which BPM and CPM are implemented, and simulates the rock domain using the interaction between an assembly of circular particles with specified statistical size distributions and bounded with four rigid walls. These particles are generated with an automatic particle generator with radii being distributed either uniformly or according to a Gaussian distribution.

Once the bond is installed between the particles, the overall mechanical behaviour of the assembly is dominated by the micro-properties of both the particles and bond. The standard process of generating a PFC2D assembly to represent a preliminary test model of a rock-like specimen includes particle generation, packing the particles, stress initialization, floating particle elimination and bond installation (Itasca Consulting Group 2008; Wang et al. 2003).

The ultimate mechanical behaviour of the bonded particles assembly in PFC2D is described by the movement of each particle and the force and moment acting at each contact. The fundamental relation between particle motion and the resultant forces and moments causing the motion is provided by the Newton's laws of motion (Itasca Consulting Group 2008). By modelling a rock-like sample as a collection of separate particles bonded together at their contact points, the simulated material can develop cracks as bonds between the particles break under normal and shear loads. Particles are assumed to be rigid in PFC2D, but the deformability of the assembly is derived from normal and shear bonds. Each bond also has a strength that represents intact bonding (cohesive strength). The bond that is broken carries no tension when either a tensile or a shear force limit is reached (Itasca Consulting Group 2008).

This paper is to simulate the shearing behaviour of rough rock fractures in a PFC2D assembly. A fracture is modelled as an interface between two opposite blocks along which the particles are initially unbounded, as shown schematically in Fig. 1. By performing different and specific simulations, PFC2D is shown to simulate in a realistic manner the effects of fracture roughness, boundary loads, and more specifically contact asperity degradation. Also tracking the propagation of bond breakage (i.e. extent of damage zone) is shown to be possible.

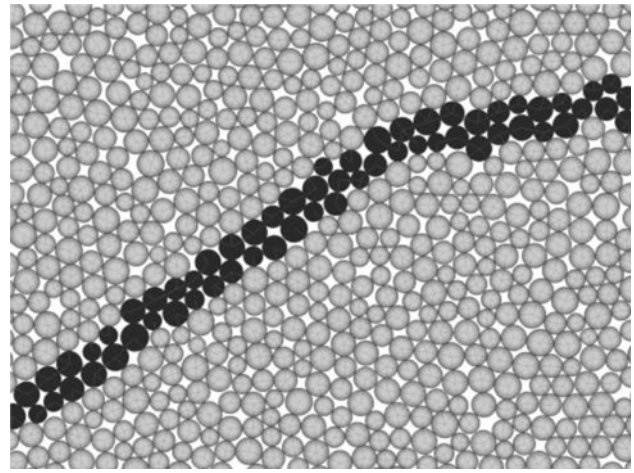

Fig. 1 PFC2D example model of a rough fracture track (*unbonded black balls*), bonded particles (*gray balls*), and contact bonds (*dark gray lines*) shown in the model

2.1 PFC2D Modelling: Specifications and Limitations

The main advantage of PFC2D in the simulation of the mechanical behaviour of a rock-like assembly is that the rock is modelled at a micro-scale. As a result, investigation of micro-fracturing and micro-damage of rock becomes possible. However, as with other numerical methods some difficulties are associated with the discrete element method (DEM) which is applied with PFC2D. For instance, the rock cement is not present and its properties contribute to the simulation of the force–displacement relations.

On the other hand, all the particles are treated as discs of unit thickness, whereas in reality rock grains may have any angular shape which, in turn, can cause changes in the rock behaviour. Furthermore, the particles used in PFC2D are rigid bodies, which never fail mechanically during simulation. Rock grains, however, have limited strength and may fail. In addition, in a blocky system modelled with PFC2D the block boundaries are not planar, and the bumpiness affects the fracture response (Asadi 2011; Ivars et al. 2008). To overcome such a shortcoming, in this paper the contact bond was used and the particle size was reduced so as to minimise the effects of non-planarity of the block boundaries.

In PFC2D, the rock is modelled using a large number of bonded particles. Therefore, induced micro-fractures and damage can be studied at the micro-scale. DEM is indeed more efficient in modelling granular rock type materials than the finite element method (FEM) and continuum modelling. It is to note however that PFC2D modelling is essentially two-dimensional and is unable to realistically represent the 3D nature of rock behaviour. While 3D simulation would be possible with, for example, the PFC3D code (Itasca Consulting Group 2008), which

extends to 3D the concepts applied in PFC2D, the computational effort required made it advisable for the purpose of this paper to use 2D modelling.

Moreover, a careful selection of the micro-properties is required to represent the real rock behaviour. These are initially unknown and need be defined by using available literature data and by performing "trial and error" simulations. Accordingly, a calibration process is required until the macro-scale response of the PFC2D model is similar to the results of laboratory tests (Cundall 2000; Park and Song 2009; Yoon 2007). Many researchers have in fact attempted to calibrate the model uniaxial compressive strength, Young's modulus, and Poisson's ratio with the measured laboratorial test results (Cho et al. 2008; Potyondy and Cundall 2004; Yoon 2007). It is noted however that there are few difficulties which need be considered (Itasca Consulting Group 2008; Yoon 2007).

3 Estimation of Material Properties

A good understanding of the mechanical properties of intact rock is required before simulation of a shear test in PFC2D. The macro-properties of the specimen are not known at the beginning of simulation and there is no explicit method to estimate them. Actually, an analytical-statistical method has been proposed to define the model micro-properties, which need be calibrated with laboratory experiments to obtain the macro-properties (Yoon 2007). A good approach is to simulate biaxial and Brazilian tests to estimate the specimen macro-properties including Young's modulus, Poisson's ratio, uniaxial compressive strength, tensile strength, cohesion and internal friction (Jing and Stephansson 2007; Koyama and Jing 2007; Potyondy and Cundall 2004).

In this section, the set up of a biaxial test with PFC2D is briefly described and the method for determining the macro-properties from the simulations is illustrated. Then several biaxial tests are simulated by setting certain values for the micro-properties and analysing the influence of them on the macro-properties. Linear correlations are developed between micro- and macro-properties which will be used later for generating the specimens with given properties. Table 1 gives four data sets of the micro-properties used in the simulations (A, B, C, and D).

It is noted that the procedure for model generation and isotropic stress initialisation is similar to that to be used in the following for direct shear test simulations. Biaxial tests are simulated in a 2D box with 5 cm width and 10 cm height, where the upper and lower walls of the specimen are given a prescribed constant velocity in the vertical direction (here 0.1 m/s) so as to achieve a compression of the sample while the stress on the left and right walls is

Table 1 Sensitivity analysis of micro-properties in PFC2D biaxial test simulation: the range of values used for each property is marked in *bold*

Data set	Micro-property	Particle average radius (mm)	Number of particles	Contact bond strength (MPa)	Contact elastic modulus (GPa)	Ratio of normal to shear stiffness	Altered macro-parameter
A-1	Particle average radius	**0.993**	**1,400**		1.25	2.5	
A-2		**0.745**	**2,489**				
A-3		**0.496**	**5,602**				
A-4		**0.372**	**9,959**				
A-5		**0.257**	**20,000**	60	1.25	2.5	
B-1	Contact bond strength	0.993	1,400	**10**	1.25	2.5	UCS
B-2				**20**			
B-3				**30**			
B-4				**40**			
B-5				**50**			
C-1	Contact elastic modulus	0.993	1,400		**1.25**	2.5	Young's modulus
C-2					**5**		
C-3					**10**		
C-4					**15**		
C-5					**20**		
D-1	Ratio of normal to shear stiffness	0.993	1,400		1.25	**0.1**	Poisson's ratio
D-2						**1.0**	
D-3						**2.0**	
D-4						**3.0**	
D-5						**4.0**	

kept constant and equal to the initial stress value, by using a servomechanism algorithm as developed by Itasca Consulting Group (2008), at the initial stress value. The biaxial test simulations were performed under unconfined conditions ($\sigma_c = 0$) and three different confining stresses ($\sigma_c = 10$, 20, and 30 MPa).

Table 1 shows the range of different micro-properties used for the biaxial test simulations. In each case, one micro-property (particle average radius, contact bond strength, contact elastic modulus, and ratio of normal to shear stiffness) is changed while others are kept constant in order to obtain meaningful correlations between the model micro-properties and macro-properties as shown in the last column of Table 1.

3.1 Uniaxial Compressive Strength

Based on the behaviour of a particle flow system, the uniaxial compressive strength (UCS) is found to be highly dependent on the strength that a bond can carry, either under normal and/or shear loading. A linear regression fit is obtained between UCS and the contact bond strength (CBS) through a series of biaxial compression test simulations by varying CBS from 10 MPa up to about 60 MPa. Typical UCS values for soft rocks in the range 20–80 MPa are assumed.

As shown in Table 1, in data set B the CBS is increased from 10 MPa up to 60 MPa. Since the bonds act as cement between the rock grains, larger UCS values are expected as CBS increases. Correspondingly, the Young's modulus and Poisson's ratio are expected to remain constant as CBS changes. From the stress–strain curves, the UCS versus CBS relationship is obtained and a linear correlation is found as follows:

$$\mathrm{UCS} = 1.3269\mathrm{CBS} + 0.747. \quad (1)$$

which can be used to estimate the specimen UCS given CBS.

Furthermore, the particle size can also affect the UCS values, as different particle sizes result in different porosity and packing density in the specimen being modelled. To assess this effect, a number of biaxial tests were simulated with different particle size. Data set A in Table 1 shows the input values for this model in which the average particle radius varies from 0.4 to 1.2 mm. A linear correlation is obtained between UCS and R_{ave} as follows:

$$\mathrm{UCS} = -27.645R_{ave} + 43.812. \quad (2)$$

which can be used to estimate the intact specimen UCS as a function of R_{ave}.

However, a relevant point to raise here with reference to the above correlations deals with the ratio of the model compressive strength to the tensile strength. Generally, the tensile strength is obtained from Brazilian test simulations in PFC2D (Itasca Consulting Group 2008). For example, Yoon (2007) obtained ratios ranging between 2.4 and 5.2, which are much smaller than commonly observed in typical crystalline and sedimentary rocks (i.e. 5–10 or 20).

Bruno and Nelson (1991) stated that modelling grains with circular disc-shaped particles produces an assembly where the compressive loads are distributed differently than an assembly consisting of more angular grains. They suggested the use of clumped particle models clustered together with specified bond strength to represent angular or blocky grains (Cho et al. 2007) in order to reproduce realistic ratios of compressive to tensile strength.

On the other hand, the use of a bonded clump model to simulate fracture shear strength is not straightforward. Potyondy and Cundall (2004) and Yoon (2007) stated that the ratio of UCS to the Brazilian tensile strength of bonded particle models should be between 3 and 10. To obtain the reasonable values in the above range, the ratio of the shear bond strength to the normal bond strength should be between 1 and 3. This is the range considered in this paper (see Table 2).

3.2 Young's Modulus and Poisson's Ratio

In DEM the Young's modulus of the assembly E is a function of the contact elastic modulus E_c. To investigate this, biaxial tests were simulated according to data set C in Table 1. It is observed that the modulus of a two-dimensional assembly is directly proportional to the contact stiffness, but is independent of the particle radius. The linear correlation obtained is as follows:

Table 2 PFC2D model micro-properties and corresponding macro-parameters used in fracture shear test simulations

Property	Value	Assembly's macro-properties
Sample size, width × height (cm^2)	10 × 5	$E = 1.00 \pm 0.25$ (GPa)
Particle density (kg/m^3)	1,000	$\nu = 0.300 \pm 0.015$
Minimum particle radius, R_{ave} (mm)	0.257	UCS = 40 ± 3 (MPa)
Particle size ratio, R_{max}/R_{min}	1.5	$c = 14 \pm 2$ (MPa)
Porosity, n	0.12	$\phi = 24 \pm 2$ (°)
Number of particles	20,000	
Contact elastic modulus (GPa)	1.25	
Contact stiffness ratio, k_n/k_s	2.5	
Particle friction coefficient, μ	0.6	
Normal bonding strength, NBS (MPa)	60	
Shear bonding strength, SBS (MPa)	60	

$$E = 0.5564E_c + 0.0742. \quad (3)$$

which can be used to estimate E given E_c. However, care must be taken since the micro-parameters used in PFC2D are dependent on each other and therefore changing one parameter may influence the overall macro-response of the model.

A point of relevance in the study of two-dimensional contact models is the relationship between the E_c and the normal secant stiffness k_n which is defined as:

$$k_n = 2E_c(t). \quad (4)$$

where k_n relates the total normal force F_i^n to the total normal displacement U_n:

$$F_i^n = k_n U_n n_i. \quad (5)$$

where n_i is the unit normal vector to the contact plane.

It is noted that also defined is the tangent shear stiffness k_s which relates the increment of shear force ΔF_i^s to the increment of shear displacement ΔU_i^s:

$$\Delta F_i^s = k_s \Delta U_i^s. \quad (6)$$

Considering Eqs. 5 and 6, the ratio of normal to shear stiffness is given as:

$$k_n/k_s = \frac{F_i^n \Delta U_i^s}{\Delta F_i^s U_n n_i}. \quad (7)$$

The increment of shear displacement over total normal displacement at the micro-scale can significantly change the ratio of radial to axial strain at the macro-scale, i.e. the Poisson's ratio of the 2D assembly. Based on a sensitivity analysis a relationship between the k_n/k_s ratio versus the Poisson's ratio of the assembly is obtained, which shows that the larger the ratio of normal to shear stiffness, the greater is the Poisson's ratio.

It is also to be noted that the stress conditions in a two-dimensional PFC2D test are neither plane strain nor plane stress since there is no "out of plane stress" or "out of plane deformation" (Itasca Consulting Group 2008). Thus, the Poisson's ratio ν', calculated from a biaxial test simulation with PFC2D, represents the special case of plane stress (with $\sigma_z = 0$) and constant lateral stress and is not strictly comparable to the Poisson's ratio ν obtained from a triaxial test.

A linear correlation was obtained between ν and k_n/k_s as follows:

$$\nu = 0.0937(k_n/k_s) + 0.0668. \quad (8)$$

which can be used to estimate ν versus k_n/k_s.

Interestingly, it is also observed, as shown in Fig. 2, that as k_n/k_s increases, the elastic modulus of the assembly decreases. This is due to a reduction in shear stiffness as the ratio of k_n/k_s increases. A linear correlation was derived between E and k_n/k_s as follows:

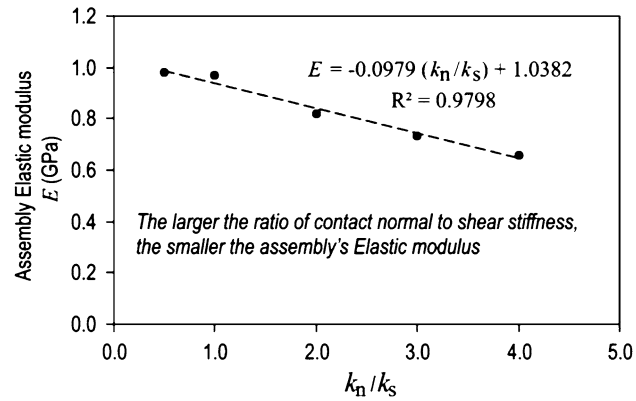

Fig. 2 Effects of contact normal to shear stiffness on 2D assembly's elastic modulus

$$E = -0.0979(k_n/k_s) + 1.0382. \quad (9)$$

which can be used to obtain E given k_n/k_s.

3.3 Intact Rock-Like Failure Mechanism

Biaxial tests were also simulated with confining pressures of 10, 20 and 30 MPa, respectively. Figure 3 shows the specimen after the test, where the lighter gray and white zones represent planes of shear failure. It is seen that the failure pattern is nearly the same for different confining pressures. Also, larger lateral displacements are observed in the specimen for the unconfined tests compared to the confining pressure tests. As expected, the number of shear cracks increase as the confining pressure reduces (note that the density of the white colours in the samples, which shows the extent of the broken contact bonds, reduces as the confining pressure increases).

The Mohr's circles corresponding to the biaxial tests simulated are plotted in Fig. 4. The diameter of each circle is equivalent to the difference between the two stress components at the point of failure (σ_1 and σ_3). From the tangent line to these circles the friction angle and cohesion of the simulated rock-like material can be estimated to be $(24 \pm 2)°$ and (14 ± 2) MPa, respectively.

Table 2 gives the selected micro-properties used in the shear test simulations and the corresponding macro-properties estimated. This data set was used for modelling mainly because the values of the parameters are within the range of values used by other researchers in fracture shearing studies (Asadi and Rasouli 2010, 2011; Cundall 2000; Park and Song 2009; Potyondy and Cundall 2004; Rasouli and Harrison 2010).

4 Fracture Shearing Simulation Using PFC2D

The shear behaviour of a rock fracture depends on the effective normal stress acting perpendicular to the fracture

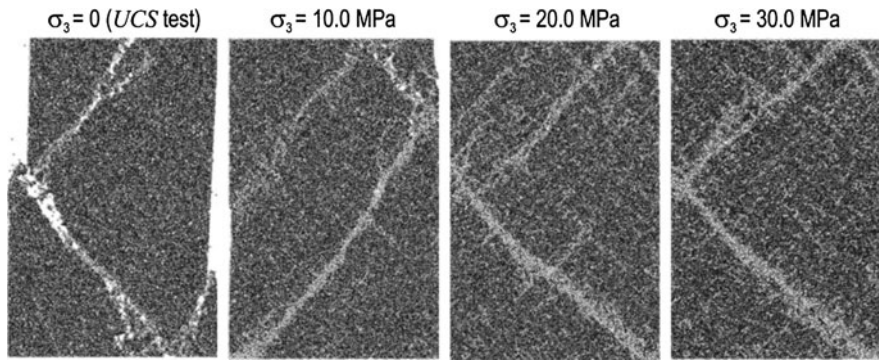

Fig. 3 Assembly of balls and contact bonds after biaxial tests simulation under unconfined, and confining pressures of 10, 20, and 30 MPa

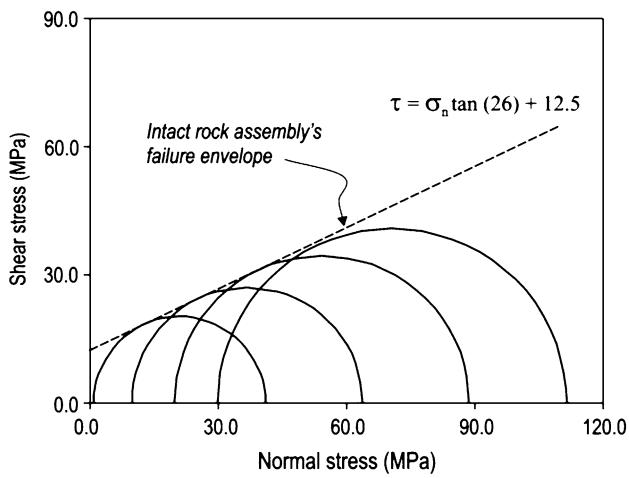

Fig. 4 Mohr circles corresponding to biaxial test simulations at different confining pressures

plane. At low normal stress, sliding occurs along an inclined surface with minor asperity damage. At high normal stress, however, the constraint of normal displacement leads to asperity failure. With this in mind, a number of synthetic and rock fracture profiles in a rock-like specimen were modelled in PFC2D.

A total number of 20,000 particles with an average radius of 0.257 mm were generated and packed into a $10 \times 5\ \text{cm}^2$ box-shaped model containing 4 walls, as shown in Fig. 5a. In order to avoid packing, the particle radii were chosen to be randomly distributed between a minimum and a maximum particle radius. Once the assembly of particles was completed with no further particle floating, a stress of 0.1 MPa was applied. Figure 5b shows that the contact normal and shear forces are distributed uniformly in the assembly once an equilibrium state is reached.

To create a fracture in the model, a 2D profile was inserted in the centre of the shear box using a defined function $y = f(x)$ or coordinate points x and y representing the chosen profile. Zero contact bond strength is assigned to all the particles between the upper and lower walls of the fracture. A very low (0.05) particle friction coefficient was

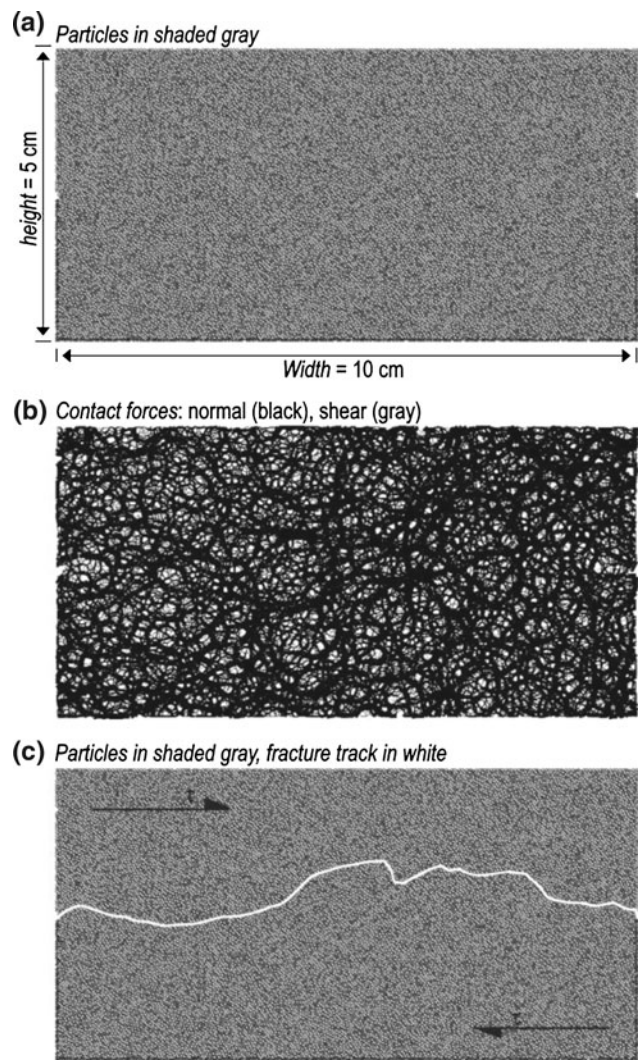

Fig. 5 **a** PFC2D representation of a rock-like assembly with 20,000 discs of unit thickness, **b** contact force distribution, **c** rough fracture profile generated in the centre of the model

given to all the unbonded particles (known as fracture particles) between fracture walls (see Sect. 4.3). The coordinates of the desired fracture profile in a particular direction must be digitised at sampling intervals smaller than R_{ave} (here 0.257 mm) to reproduce a high resolution

fracture in the PFC2D model accounting for both roughness and waviness.

4.1 Bonding Type

The effect of bonding on the fracture shear behaviour was previously studied by Park and Song (2009) who simulated direct shear tests. The micro-properties of two models, one with contact and the other one with parallel bonds, were considered. Small differences in the peak shear strength, normal dilation and shear stiffness were obtained from the two models with different bonding types. It was observed that more micro-cracks develop along the fracture plane, with a residual state being reached faster than with the contact-bonded model. In addition, when studying the asperity degradation during fracture shearing, micro-cracks were observed to develop through asperity contacts and intact blocks.

For the purpose of this study, normal and shear bond strengths were distributed uniformly in the shear box in order to ensure a consistent response under different loading conditions and fracture geometries. Failure to do so may result in some damage occurring where bond strength is distributed non-uniformly. Furthermore, in order to prevent spurious failures at the boundaries, the strength contacts adjacent to the top and bottom edges of the shear box were increased by a factor of 10 (Cundall 2000). In fact, a low strength assigned to the contacts at the box boundaries would result in shearing energy being dissipated due to large tension cracks initiating from doglegs of asperities and propagating to shear box boundaries.

4.2 Particle Size Distribution

A fracture plane in the PFC2D model has an intrinsic roughness even if it is planar. This is due to a different size distribution of the particles along the fracture plane. The micro-roughness increases along the fracture as the particle size increases, so that by reducing the particle size in the model, this effect becomes less important. However, the fracture compressive strength will decrease with increasing the particle size due to the reduction in the number of fracture-contacts.

To minimise the effects of intrinsic roughness (or say micro-roughness), as shown in Fig. 6, a dense pack of particles was used with small size particles radii (R_{ave} 0.257 mm). As shown by Potyondy and Cundall (2004), the particle size affects the fracture toughness and influences the damage process (such as notch formation). Damage is localised at the macro-fracture tips and experiences extensile loading.

By changing the number of particles in the assembly, the mean particle radius will change, thus affecting the ultimate response of the model. Generally, the variation of the results in the models with different mean particle size is due to the change of porosity and therefore of the uniaxial compressive strength of the assembly, as shown through biaxial test simulations.

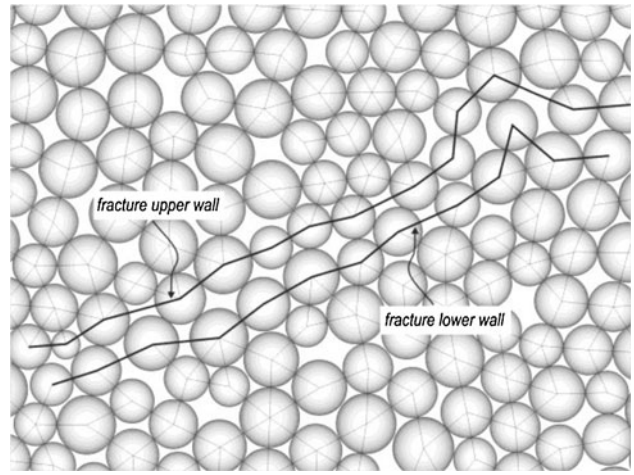

Fig. 6 Unbounded path of particles represents a rough fracture profile

To investigate the effects of particle size on rough fracture shear behaviour, five sets of shear test simulations were performed with similar micro-properties for all the models shown in Table 2. Different numbers of particles with different particle radii were used. The mean particle radius was varied between 0.1 and 1.0 mm, which represents the range of small to medium sand grains.

Then a symmetric triangular profile (i.e. a crenulated profile) with base angle $\theta = 30°$ was generated in the centre of the model to investigate the effects of particle size on shear strength. Figure 7 shows the PFC2D model of the profile sheared under 5.0 MPa normal stress for three assemblies with 0.257, 0.431, and 0.647 mm average particle radius, respectively. It is seen, as expected, that by reducing the particle size, since the number of particles increases in the model, a finer failure pattern is observed.

Figure 8 shows the peak shear stress versus the mean particle size for the normal stress equal to 5.0 MPa. The peak shear stress reaches a maximum for a mean particle radius equal to 0.6 mm, then to decrease due to a significant reduction in matrix strength. A similar trend was obtained for the normal stress equal to 1.0 and 10.0 MPa. This variation in shear strength can be due to the superposed effects of the inherent roughness (bumpiness) of the fracture surfaces, as already discussed. Hence, local particle contact orientations along the fracture surface may cause significant changes in fracture shear strength. It is seen that the peak shear stress reduces with $R_{ave} \leq 0.4$ mm, due to the reduction in strain localisation in particles along the fracture.

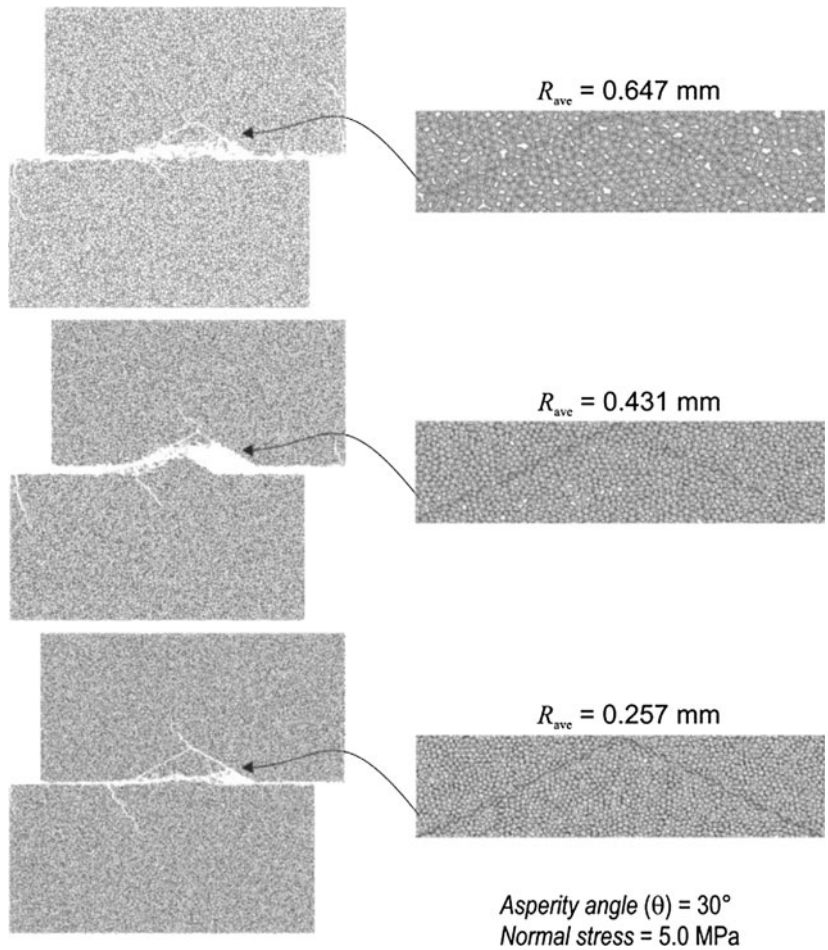

Fig. 7 Visual demonstration of fracture micro-roughness corresponding to various particle sizes

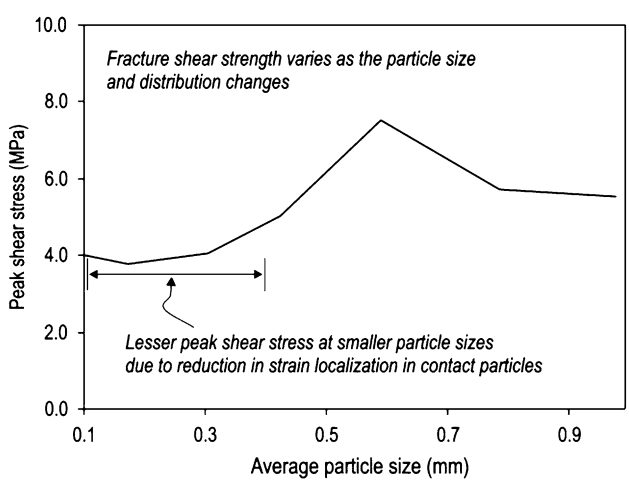

Fig. 8 Effects of particle size on peak shear stress of a symmetric triangular asperity profile depicted in Fig. 3.13

Therefore, to simulate the shearing of rough fractures, i.e. the influence of fracture geometry on the shear behaviour, it is advisable to decrease the particle radius in order to reduce the effects of fracture micro-roughness. In this study, as the major focus is on fracture surface geometry (i.e. on both waviness and roughness), the average particle size R_{ave} was set to be 0.257 mm. It is also noticed that, if $R_{ave} \geq 0.7$ mm, the peak shear strength is influenced more by the significant decrease in fracture compressive strength than by the increase in fracture surface roughness. Although, these examples and the results obtained are case specific, a similar concept is applied to fractures with different geometries modelled in this way.

4.3 Fracture Particles Friction Coefficient

The shear strength of a fracture modelled in PFC2D is affected by the friction coefficient of the unbonded particles along the fracture plane (Cundall 2000; Lambert et al. 2010; Park and Song 2009). When the bonded particle model is used with no bond between the particles (when the existing bond is broken), the friction coefficient controls particles sliding. Therefore the value of the friction coefficient of the particles on the opposite sides of a fracture is of major importance and is to be correlated to the basic friction angle of the planar fracture being simulated, which is assumed to be equal to 30°.

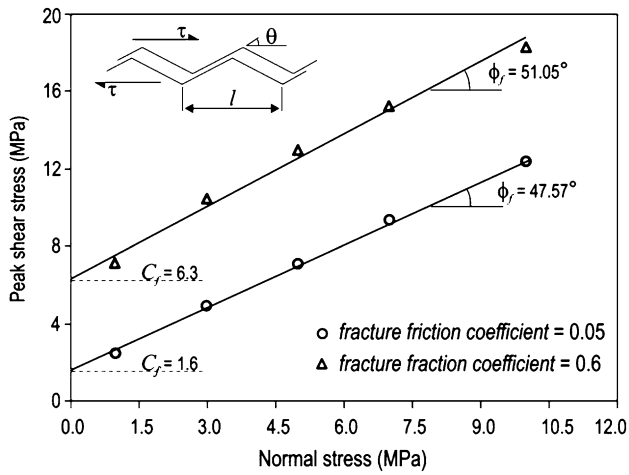

Fig. 9 Effects of particle friction coefficient on peak shear strength of planar and rough fractures

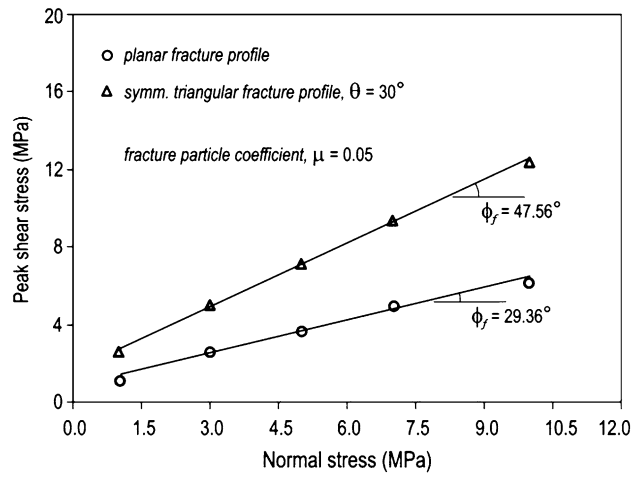

Fig. 10 Effects of particle friction coefficient on peak shear strength of planar and rough fractures

To understand the influence of the fracture particle friction coefficient on the shear behaviour of planar and rough fractures, two sets of PFC2D shear tests were simulated under the same conditions but with different particle friction coefficients equal to 0.05 and 0.6 respectively. Shear test simulations were performed for a planar fracture as well as a rough fracture with symmetric triangular profile of 30° asperity angle, as shown in Fig. 9, where the peak shear strength versus normal stress diagram is plotted for the two different friction coefficients. It is observed that for rough fractures, a significant increase in the particle friction coefficient from 0.05 to 0.6 causes only a small increase in the fracture angle from 47.57° to 51.05°, whereas the apparent cohesion increases significantly from 1.6 to 6.3 MPa (Asadi 2011; Asadi and Rasouli 2011).

The effects of the fracture profile roughness with particles characterised by a very small friction coefficient (0.05) on the fracture shear behaviour was investigated by simulating a planar and a rough (i.e. 30° symmetric triangular profile) fracture profile. The results show that the fracture friction angle and cohesion become greater with the fracture roughness increasing. The friction angle is found to change from 29.36° to 47.56° as the cohesion increases from 0.912 to 1.6 MPa (Fig. 10).

These results show that for JRC > 12 (i.e. for rough fractures) the roughness has larger effects on cohesion than friction angle has. This is like to say that the value of the particle friction coefficient does not significantly change the mechanical shear behaviour of the fracture. Large values of the fracture friction coefficient will result in overestimation of the apparent cohesion and in turn of the peak shear strength, as illustrated in Fig. 10.

4.4 Boundary Conditions and Stress Calculations

In the models presented in this paper, the normal load is applied vertically to the upper block. To simulate a direct shear test under constant normal load (CNL), the upper block is allowed to move vertically over the lower one (i.e. dilatation is permitted). This is controlled by a numerical servomechanism in the PFC2D model, which keeps the vertical reaction force constant at some specified values of the normal load (Itasca Consulting Group 2008). Horizontal shear displacements are then applied by imposing a velocity to the elements of the upper block so as to displace against the lower one, which is kept fixed.

The boundary particles comprising the upper and lower blocks of the shear box are controlled to perform the shear test. After deleting the walls, all the particles existing in the model are divided into two groups, those located above and below the fracture profile. This allows one to control the upper and lower blocks independently. The lower block is kept stationary throughout the test, and the upper block is translated as a rigid body with constant velocity (i.e. shearing rate) in the horizontal (shearing) direction.

Shear and normal loads are applied by giving horizontal and vertical velocities to the upper block. Both normal and shear forces on the upper block are evaluated continuously. The shear stress is calculated by dividing the average shear force of the upper and lower blocks by the fracture width. A similar procedure is applied to evaluate the normal stress, which is obtained by dividing the average normal force applied to the upper and lower blocks by the shear box width. The vertical displacement is controlled by a numerical servomechanism described in the PFC2D user manual (Itasca Consulting Group 2008).

The specimen is loaded by specifying the velocities of the top and bottom block particles. During the loading process, the normal stress is kept constant by means of a numerical servomechanism that is implemented by a servomechanism function and a gain parameter. This function determines the stresses and uses a numerical servocontrol to adjust the upper block velocities and reduce the difference between the measured and the required force. Based on the servomechanism implemented in the model, the following equation gives the velocity of the blocks as:

$$u = G\left(f_{\mathrm{n}}^{\mathrm{measured}} - f_{\mathrm{n}}^{\mathrm{required}}\right). \tag{10}$$

where G is the "gain" parameter that needs to be adjusted for different applications based on time steps and contact force area (Itasca Consulting Group 2008).

In current simulations, the shearing velocity was set to 0.3 m/s and the gain parameter was chosen in the model for both the vertical and horizontal directions to ensure a constant normal stress throughout the test with a constant velocity. Displacements were calculated based on the assumption that velocities are constant in each time step. Having the values for time step and velocity, displacements can be calculated in both vertical and horizontal directions.

Histories of shear stress, normal stress, and shear and normal displacements were recorded in each time step to enable one to plot the shear stress versus shear displacement and normal displacement versus shear displacement curves. It is widely accepted that by increasing the shearing rate, the shear strength of fractures increases. In this study, a large number of shearing cycles was applied to capture the post-peak behaviour of fracture profiles. A 3.0 mm shear displacement allowed for fractures with 10.0 cm width to undergo a complete failure cycle including the post-peak region.

4.5 Development of Cracks

The advantage of using PFC2D in the study of fracture shearing is that complex failure phenomena in pre- and post-peak stress behaviour of intact rocks can be simulated and the entire process of crack initiation, growth, coalescence, localization and complete breakdown can be visualised without requiring continuous system re-configuration.

Preliminary simulations were performed on the rock fracture profile shown in Fig. 5c with the aim of tracing the process of micro-cracking (i.e. failure pattern) under different normal stress. Figure 11 shows the profile after shearing under 3.0 and 7.0 MPa normal stress, respectively. Shear failures are shown in gray and tensile cracks in black. It is seen that at low normal stress (3.0 MPa) sliding is the dominant failure mechanism (Fig. 11a) as local shear failures are only concentrated around the asperity contacts.

Small tensile cracks also develop at profiles doglegs. In comparison, at high normal stress (7.0 MPa), the amount of contact shear failure reduces but large tensile cracks develop at asperity doglegs, with either asperity cut-off or intact rock failure (Fig. 11b). It is noted that in this case dilation decreases significantly due to the concentration of compression forces on the shearing chord of the fracture profile as the accumulated force tries to open a large tensile crack.

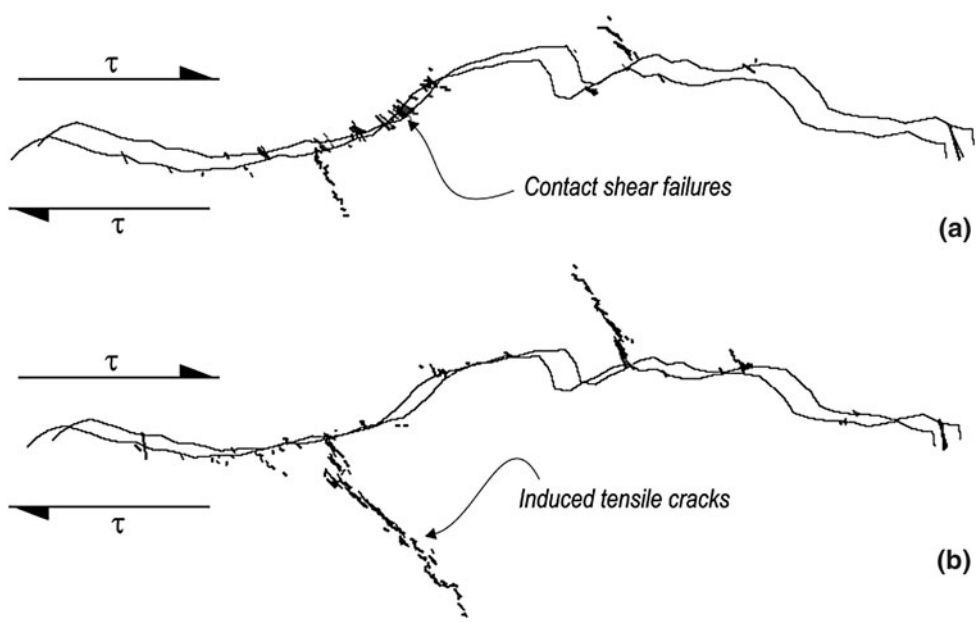

Fig. 11 Micro-cracking pattern after rough fractures shear test in PFC2D at (**a**) 3.0 MPa and (**b**) 7.0 MPa normal stress; shear displacement is 3.0 mm

5 Shearing Simulation of Synthetic Profiles

Following the presentation of an analytical solution used to estimate the asperity cut-off strength for symmetric triangular fractures, synthetic and rock fracture profiles are considered in PFC2D shear test simulations.

5.1 Fracture Contact Asperity Cut-off

Huang et al. (2002) proposed a simplified analytical model to estimate the shear strength of a synthetic crenulated profile with symmetric triangle asperities, as shown in Fig. 12. This model was developed based on the Mohr–Coulomb failure criterion and the limit equilibrium method by considering the normal and shear forces acting on the asperity contacts. Direct shear tests on artificial fractures with symmetric asperities were also carried out in the laboratory and validated with the model.

Figure 13 shows a shear box containing a symmetric triangular profile with angle θ, chord length s, and asperity base length L in a material that obeys the Mohr–Coulomb failure criterion. This profile is subjected to both a horizontal shear stress τ acting from left to right and a normal stress σ_n applied vertically. The stiffness of the system is assumed to be sufficiently high to ensure that failures occur at the asperities upslope (i.e. chord s).

The limit equilibrium analysis of the free body diagram of the broken asperity gives the resultant normal and shear forces on the cut-off plane based on the normal and shear stresses (σ_n, τ) applied to the shear box. According to the

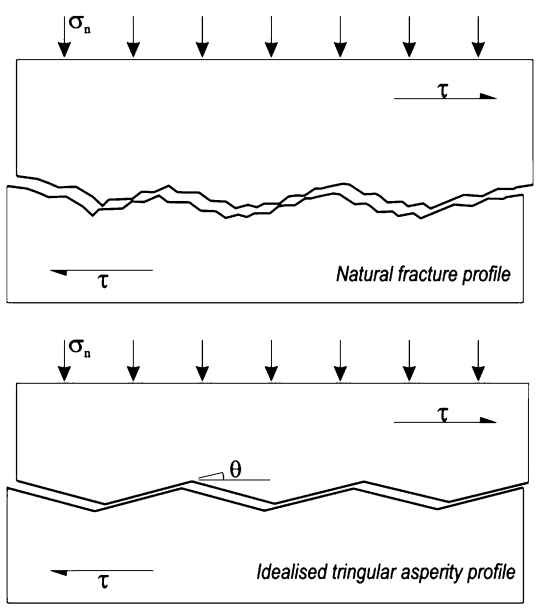

Fig. 12 Simulation of a rock fracture with an idealised triangular asperity profile (after Huang et al. 2002)

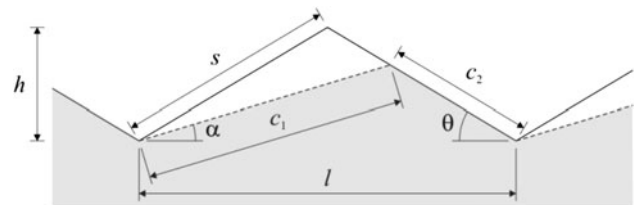

Fig. 13 Geometrical features of asperity Cut-off in a symmetric triangular profile

Mohr–Coulomb failure criterion the shear strength of the critical plane along which shear failure occurs is defined as:

$$\tau = \frac{c \sin\theta / \sin(\theta + \alpha)}{\cos\alpha - \sin\alpha \tan\varphi} + \sigma_n \tan(\alpha + \varphi), \tag{11}$$

where α is the inclination of the critical plane (found by evaluating $d\tau/d\alpha = 0$), θ is the asperity base angle, and c and ϕ are the cohesion and friction angle of the intact rock, respectively.

Equation 11 was initially developed based on the assumption that the horizontal displacement of the specimen has caused the right chord of the lower block to have previously separated from the upper matched block, and hence the forces acting on the right side chord are zero.

Figure 13 shows that after asperity failure has taken place, the profile geometry changes to an asymmetric triangular profile with angles α and θ corresponding to chords c_1 and c_2, respectively, where:

$$c_1 = l \sin\theta / \sin(\theta + \alpha) \tag{12}$$

and:

$$c_2 = l \sin\alpha / \sin(\theta + \alpha). \tag{13}$$

The normal stress above which the profile roughness will be sheared completely smooth is obtained by evaluating $(d\tau/d\sigma_n)_{\alpha=0} = 0$, which leads to:

$$\sigma_n|_{\alpha=0} = c(\cot\theta - \tan\varphi)\cos^2\varphi. \tag{14}$$

which defines the point where the fracture shear strength curve intersects the intact rock and above which the fracture roughness becomes ineffective on the peak shear strength behaviour of the fracture.

Equation 11 together with the Mohr–Coulomb model could be used to represent the shear strength envelope for a synthetic triangular fracture profile. This is shown in Fig. 14 for different profiles with increased base angles, where the corresponding asperity cut-off angles α are also plotted. It is noted that the shear strength increases as the normal stress increases and this is larger for rougher profiles (i.e. higher asperity angles).

Also shown in Fig. 14 is that the cut-off angle decreases as the normal stress increases and levels off to zero, which corresponds to a smooth surface where the asperities are

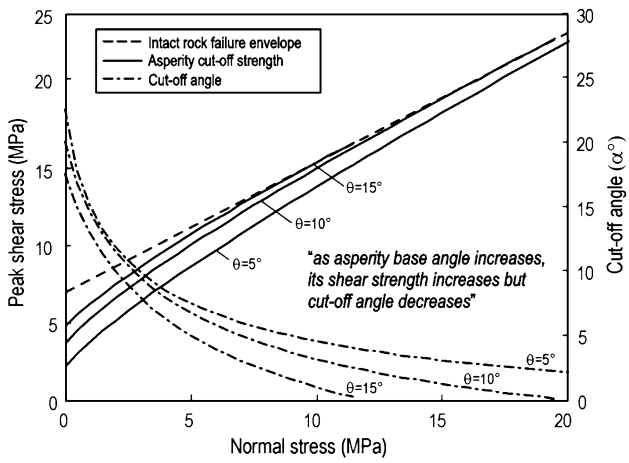

Fig. 14 Shear strength and asperity cut-off angle of synthetic symmetric triangular profiles as a function of normal stress

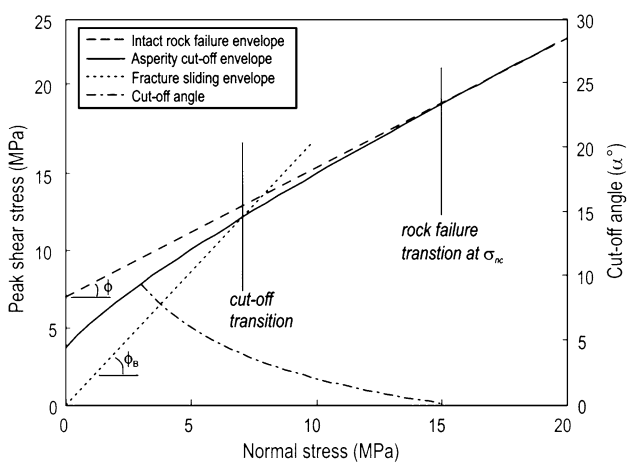

Fig. 15 Transition between fracture sliding, asperity cut-off, and intact rock failure mechanisms

sheared off from the base line. In general, the shearing process of fractures is expected to be a combination of contact sliding at low normal stresses, asperity cut-off at relatively high normal stresses, and rock failure at normal stresses larger than the critical normal stress defined using Eq. 14.

This is depicted in Fig. 15 where the transition point between the three mechanisms may vary as a function of the fracture basic friction angle and cohesion properties. It is noted that Huang et al. (2002), in laboratory experiments on two sets of artificial symmetric triangular fractures with base angle $\theta = 15°$ and 30°, evidenced four failure modes during fracture shearing: asperity sliding, cut-off, separation, and crushing. Typically, Fig. 16 schematically shows asperity sliding and cut-off for different normal stresses (Huang et al. 2002). It is seen that as the normal stress and asperity angle increase, the cut-off angle decreases until a smooth surface parallel to the fracture plane is created.

5.2 Symmetric Triangular Profile

D_{R1} is the 1D Riemannian dispersion parameter based on the multivariate analysis of the unit normal vectors to a fracture profile, which may be used to characterise its roughness. The larger is D_{R1} the rougher will be the fracture profile. It is also well understood that the larger the profile roughness, the greater will be the fracture shear strength. Rasouli and Harrison (2010) have shown the applicability of D_{R1} as a fracture roughness parameter through the analysis of synthetic and rock fracture profiles. By using a symmetric synthetic profile, they showed that a direct correlation exists between D_{R1} and fracture shear strength.

By using PFC2D simulations of fracture shear tests, as described so far, the aim is now to develop the D_{R1} concept to synthetic profiles with different geometries and also to rock fracture profiles. Symmetric and asymmetric triangular as well as sinusoidal profiles were used. Also considered were randomly generated and rock fracture profiles. By means of cubic spline fits, correlations were developed between the peak shear strength obtained from PFC2D simulations and D_{R1}.

A simple symmetric triangular linear profile with wavelength l and amplitude h, as shown in Fig. 13, is characterised by either the aspect ratio h/l or the angle θ. For this profile, D_{R1} is written as (Rasouli 2002):

$$D_{R1} = \tan^{-1}(2h/l), \tag{15}$$

which corresponds to the asperity angle of the profile.

The shearing behaviour of a synthetic profile with a symmetric triangular geometry of the asperity was simulated first with PFC2D. By assuming the asperity wavelength l to be constant and increasing the amplitude h, the effect of profile roughness can be investigated. If one takes the profile wavelength to be 2 cm, D_{R1} can be calculated based on the radians of the asperity base angle (e.g. D_{R1} for a single asperity with base angle of 30° is 0.577). Consequently, D_{R1} for any symmetric triangular profile can be readily calculated by taking the tangent of the asperity base angle θ. It is noted that asperity amplitude and wavelength have separate effects on the fracture shear strength and care must be taken when different profile shear strength values are to be compared, in which asperity amplitude h, or wavelength l, are varied.

The shear box simulated with PFC2D has the same properties given in Table 2. Simulations were performed under different normal stress values (from very small, 1.0 MPa, to very high values, 10.0 MPa), so as to plot the fracture failure envelopes corresponding to different scenarios. Figure 17 shows the PFC2D model after shearing from left to right of a symmetric triangular profile with θ equal to 15°, 30° and 45° under 5.0 MPa normal stress and

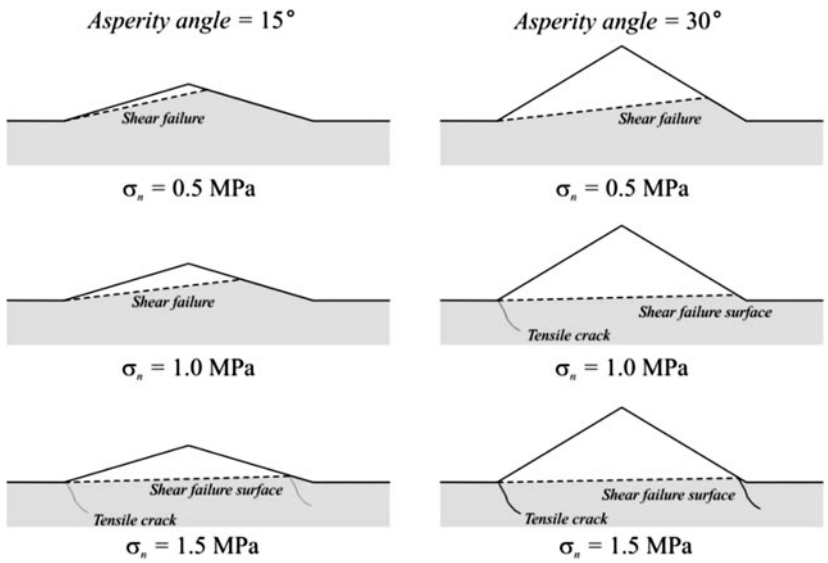

Fig. 16 Failure modes observed in direct shear experiments (after Huang et al. 2002)

by allowing for a horizontal (shear) displacement up to 3 mm, in order to be able to fully capture the deformation response of the sheared asperity. The results obtained show that asperity damage increases as θ increases, although in some cases asperity failure does not occur equally on all the asperities. This is thought to be due to the inherent roughness of the contact asperities simulated with PFC2D given the assumed particle size distribution.

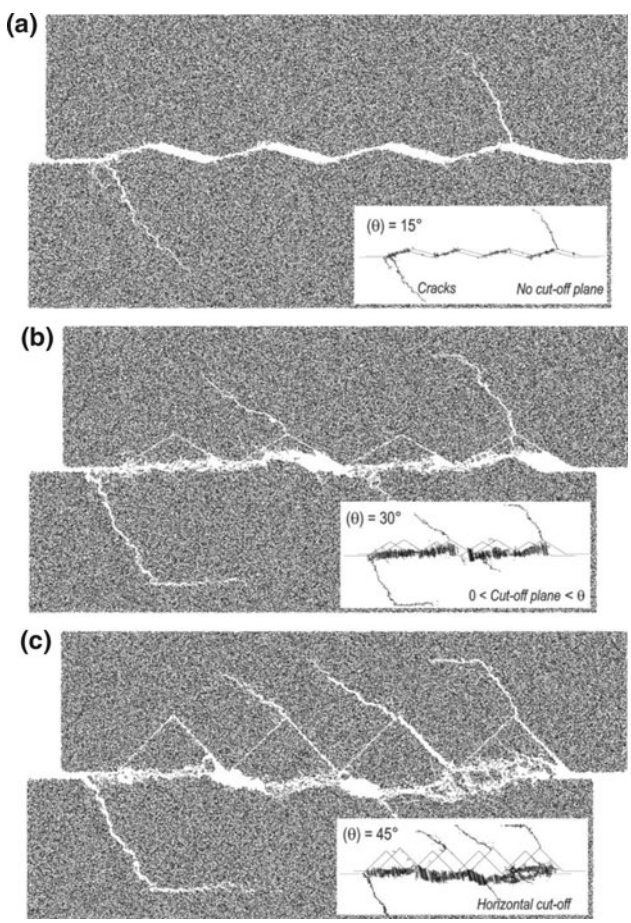

Fig. 17 PFC2D shearing simulation of symmetric triangular profiles with asperity base angles of (**a**) 15°, (**b**) 30°, and (**c**) 45° under 5.0 MPa normal stress

The cut-off planes along which the asperities are sheared off with angles less than θ are clearly visible for larger asperity base angles equal to 30° and 45°, respectively, whereas it is more difficult to recognise a cut-off plane for smaller values of θ, typically 15°. Based on this, one could argue that with low asperity angles sliding is the dominant mechanism in fracture shear testing (Fig. 17a). It is observed that the orientation of the cut-off plane is nearly horizontal under a higher normal stress regardless of the fracture morphology, given that in such a condition all the asperities fail and the effect of profile roughness becomes insignificant.

Separations are observed on the down-slope sides of the asperity contacts under both low and high normal stresses. Crushing (i.e. asperity degradation) is occasionally found to occur at the tips of the asperities (Fig. 17b). Tensile fractures are observed to initiate from the asperity tips and to develop initially at an angle nearly perpendicular to the shearing direction, followed by wing-crack type fractures propagating at approximately 45° to the shearing direction. It is noted that similar failure mechanisms have been previously reported by Huang et al. (2002) during direct shear tests of identical fractures, as shown in Fig. 16.

The residual shear strength appears to be significant since in all cases asperity degradation occurs at high normal stress and following a large shear displacement. This predominantly affects the post-peak behaviour of the fractures. Therefore, the difference between the residual shear strength of different roughness profiles can be identified based on the rate of degradation and the effectively

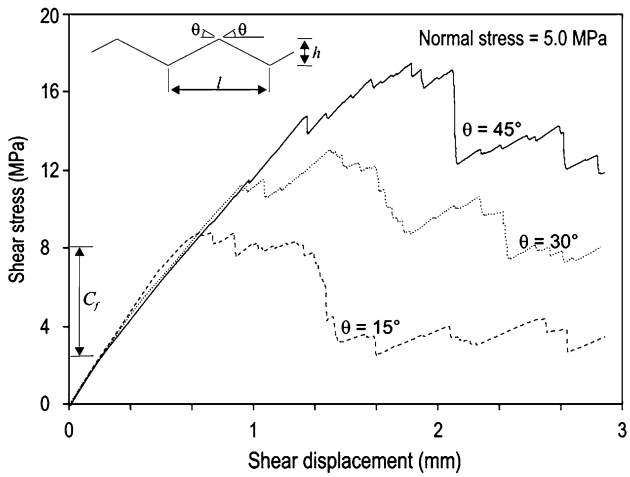

Fig. 18 Shear stress versus shear displacement curves for asperity angles of 15°, 30°, and 45° under 5.0 MPa normal stress

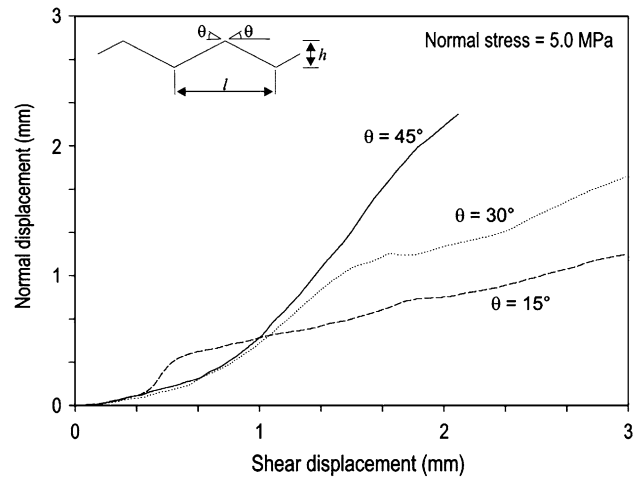

Fig. 19 Normal displacement versus shear displacement curves (i.e. dilation) for asperity angles of 15°, 30°, and 45° from PFC2D simulations

degraded area of asperity contacts. The advantage of using PFC2D in the simulation of the shear behaviour of fractures is the potential of tracing the development of microcracks at different time steps.

Figure 18 shows the shear stress versus shear displacement curves for fractures with different θ equal to 15°, 30° and 45°, respectively. It is observed that as the asperity angle increases, the corresponding peak shear strength increases. It is also noted that the difference between profiles with asperity angle of 30° and 45° is significant. This is believed to be due to the fact that, as the asperity angle becomes greater than a critical value, failure partially occurs through the intact rock, with the effect of surface roughness being reduced.

Also of interest in Fig. 18 is to compare the peak τ_p and residual τ_r shear strength values. It is noted that the difference $\tau_p - \tau_r$ decreases as the asperity base angle increases, i.e. the profile roughness becomes larger. This difference is approximately 5.5, 5.0, and 4.5 MPa for fractures with asperity angles of 15°, 30°, and 45°, respectively. This demonstrates that the chance of local asperity degradation and intact rock failure increases by increasing the profile roughness, as depicted in Fig. 17c.

Figure 19 shows the plot of the corresponding normal displacement versus shear displacement curves (i.e. dilation). A similar dilation is observed for three different asperity angles when the shear displacement is less than about 1 mm. However, as the shear displacement increases to become greater than 1 mm, dilation increases and is apparently more significant for greater asperity angles (30° and 45°). This behaviour is well described in Barton's equation (Barton and Choubey 1977) given by:

$$d_n = \mathrm{JRC}\log_{10}(\mathrm{JCS}/\sigma_n), \tag{16}$$

where d_n is directly related to the JRC value.

The effects of the normal stress on asperity shearing is illustrated in Fig. 20 where the PFC2D results are reported by giving a representation of the shearing process of the symmetric profile with asperity angle equal to 30° subjected to different values of the normal stress equal to 1.0, 3.0 and 5.0 MPa respectively. It is shown that asperity damage increases with the normal stress increasing, whereas the cut-off angle decreases. For a normal stress equal to or greater than 5.0 MPa the observed cut-off plane is nearly horizontal. This is in close agreement with the analytical approach discussed in Sect. 5.1.

Interestingly, as the normal stress increases, more asperities enter into a failure mode. For the normal stress equal to 1.0 MPa (Fig. 20a), the cut-off plane develops in two asperities only, as the other two asperities slide on the lower block. However, by increasing the normal stress to 5.0 MPa (Fig. 20c), all the four asperities are cut-off along the fracture profile. This demonstrates the significant effect of the value of the normal stress on the post-peak behaviour of fractures where both first and second order asperities are prone to fail.

The shear stress versus shear displacement curves for the symmetric profile with asperity angle again equal to 30° are plotted in Fig. 21, where also given are the corresponding normal displacement versus shear displacement curves. It is seen that the peak shear strength increases as the normal stress increases and that large differences occur in the values of dilation. It is observed that the asperities are completely sheared off with nearly no dilation taking place under normal stress equal to or greater than 15.0 MPa. Similar results have been reported by Huang et al. (2002) in laboratory shear tests showing that as the asperity base angle and normal stress increase, dilation decreases.

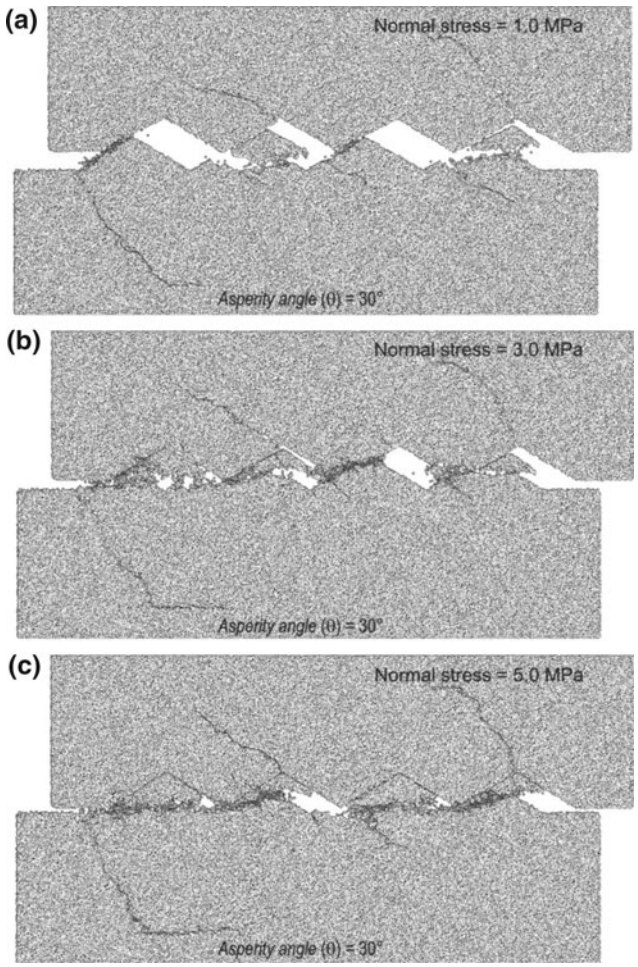

Fig. 20 Effects of normal stress on asperity shearing: **a** normal stress = 1.0 MPa, **b** normal stress = 3.0 MPa and **c** normal stress = 5.0 MPa

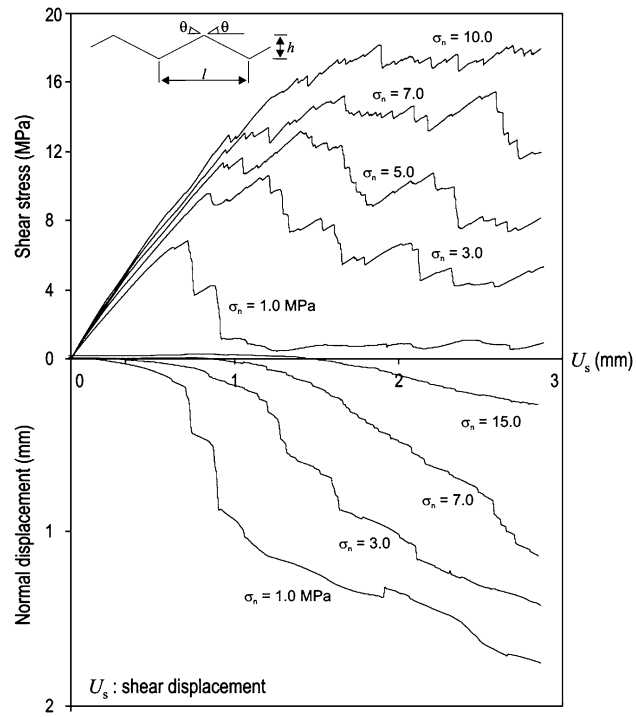

Fig. 21 Shear stress versus shear displacement and dilation curves for a profile with asperity angle of 30° under different normal stresses after 3.0 mm horizontal shearing

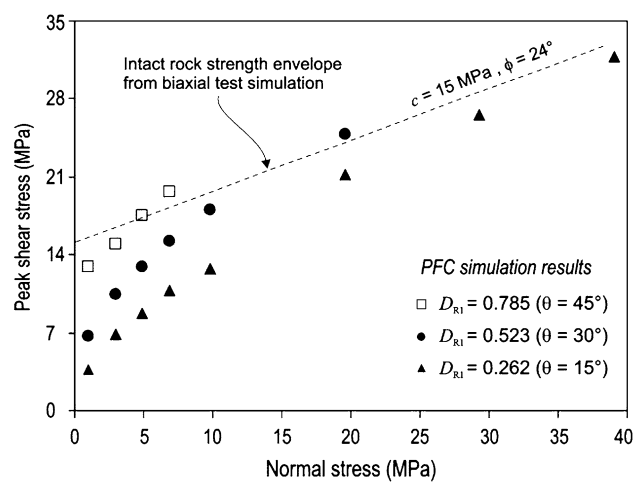

Fig. 22 Shear strength of symmetric triangular profiles with different asperity angles at different normal stresses obtained from simulation

The peak shear strength of symmetric triangular profiles with base angles equal to 15°, 30° and 45°, corresponding to D_{R1} values of 0.262, 0.523 and 0.785 respectively, are shown in Fig. 22. As expected, the results indicate an increasing shear strength with both the applied normal stress and the profile roughness increasing. It is seen that all the strength versus normal stress envelopes nearly intersect the intact rock envelope at a well defined normal stress value. Interestingly, a correlation exists between the profile base angle θ and this intersection point: as the values of θ or D_{R1} increase, the point of intersection moves to the left, i.e. failure of the intact rock takes place for a smaller normal stress or the profile roughness becomes less dominant in the failure phenomenon.

The point where the fracture shear strength envelope intersects the intact rock envelope underlines the condition above which the roughness becomes ineffective on the fracture shear strength as the profile asperities will be sheared off completely. The normal stress corresponding to this point $\sigma_n|_{\alpha=0}$ can be estimated from Eq. 14 by using the PFC2D model strength properties (c and ϕ) to obtain:

$$\sigma_n|_{\alpha=0}(\mathrm{MPa}) = 15(\cot\theta - \tan 24^\circ)\cos^2 24^\circ. \quad (17)$$

Table 3 gives the values of normal stress corresponding to the cut-off angle zero obtained from the analytical solution and simulations for fractures with asperity angles

Table 3 Normal stress corresponding to complete asperity shearing-off

Asperity base angle, θ°	$\sigma_n\|_{\alpha=0}$ from PFC2D simulations (MPa)	$\sigma_n\|_{\alpha=0}$ from analytical solution (MPa)	D_{R1}
15	40.8	41.146	0.261
30	14.9	16.109	0.523
45	5.1	6.944	0.785

of 15°, 30° and 45° are given. From this Table, a close agreement is observed between the values based on the two approaches; however, the results obtained with the numerical simulation appear to be lower than those given by analytical solution. Interestingly, as the asperity angle increases, the difference between the results obtained with the two methods becomes larger. This could be due to a more complicated failure mechanism at high normal stress, which may be either an asperity cut-off or degradation. This complexity is not adequately captured using a simple analytical formula whereas the PFC simulation might be more realistic in representing the actual behaviour.

However, it is to be noted that in real situations it is very unlikely to have rock fractures with asperity angles as high as 30° (Barton 1973; Patton 1966). The importance of this transition point, i.e. $\sigma_n|_{\alpha=0}$, is the potential of PFC2D for developing correlations between D_{R1} and the shear strength discontinuity.

5.2.1 *Effects of Contact Bond Strength*

Since the CBS and UCS values for the material used in the simulation are linearly related in a BPM, as previously discussed, and the correlation is dependent on the average particle size, the effect of CBS on the fracture shear strength was studied with a number of shear test simulations with CBS ranging between 30 and 150 MPa. The results of the sensitivity analysis performed for two different symmetric triangular fracture profiles with 15° and 30° asperity base angles under different normal stress are illustrated in Figs. 23 and 24.

Figures 23 and 24 show that the shear strength increases with the material strength in the normal stress 1–10 MPa interval. By comparing the results, the shear strength is found to be more sensitive to CBS for high normal stress values and high asperity angles (i.e. larger profile roughness). This is likely due to the extent of micro-cracking during the material bond breakage. As the chance of sliding decreases with the normal stress increasing, a large number of micro-cracks develop in the asperity contact area due to shear stress concentrations. In this condition CBS plays a more significant role in bond breakage than fracture surface properties.

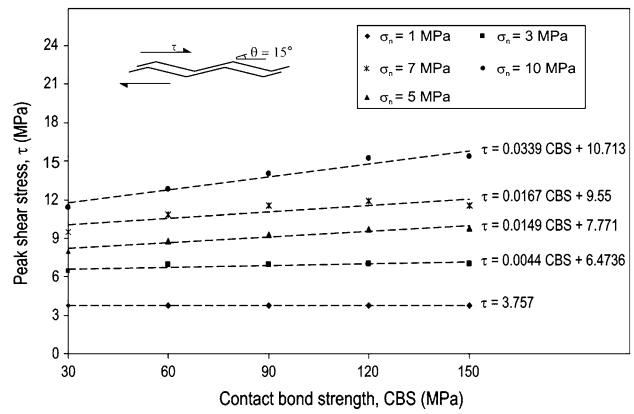

Fig. 23 Effects of CBS on peak shear stress of symmetric triangular profiles with base angle of 15° at different normal stresses

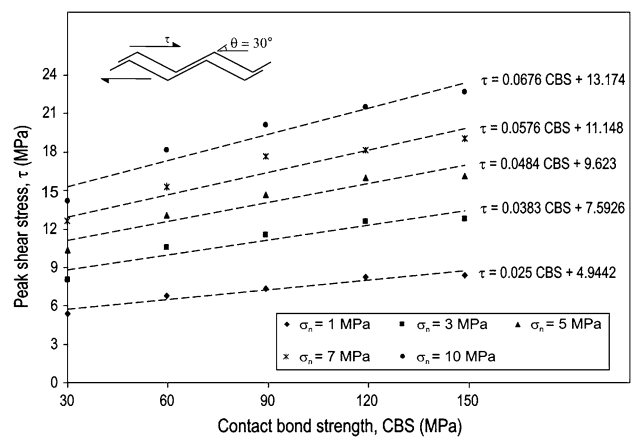

Fig. 24 Effects of CBS on peak shear stress of a symmetric triangular profile with base angle of 30° at different normal stresses

5.3 Asymmetric Triangular Profile

As shown in Fig. 25, the geometry of an asymmetric synthetic triangular profile is defined with the angles θ_1 and θ_2 corresponding to the chords c_1 and c_2 and the profile symmetry ratio l_1/l_2. Based on these characteristic values the desired profiles can be generated in the PFC2D direct shear test model and different shear test simulations can be performed, as previously done for the symmetric profiles and for a wide range of normal stress values.

Figure 26a to c show the results of the shear test simulations performed for l_1/l_2 equal to 0.25, 1.00 and 4.00 respectively, under the normal stress equal to 1.0 MPa and shearing from left to right. As expected, the pattern of behaviour is related to the asperity symmetry ratio. In Fig. 26a, for $l_1/l_2 = 0.25$ the asperities are degraded since chord c_1 acts against shearing and the upper block is hindered from moving along the lower block. Figure 26b exhibits the typical behaviour of a symmetric profile (l_1/l_2 = 1.00). In Fig. 26c, where $l_1/l_2 = 4.00$, corresponding to

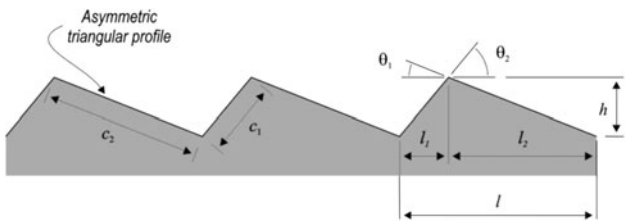

Fig. 25 Geometrical features of an asymmetric triangular profile (Rasouli 2002)

a chord c_2 smaller than c_1, sliding is observed. This indicates the directional dependency of the shear strength of an asymmetric profile, which suggests that a single roughness parameter used for estimation of the shear strength may not be appropriate but different roughness values need be used depending on the shearing direction.

Figure 27a gives the shear stress versus shear displacement curves for the same profiles as above (l_1/l_2 = 0.25, 1.00, and 4.00) and the normal stress equal to 1.0 MPa, whereas Fig. 27b shows these curves for different normal stress values from 1.0 to 10.0 MPa and the profile with l_1/l_2 = 0.25. In all cases, shearing takes place from left to right. It is seen that the peak shear strength increases with the profile symmetry ratio decreasing and the post-peak behaviour exhibits significant changes. Also, the peak shear strength and the amount of degradation increase with the normal stress increasing, with a higher normal stress associated with a residual state being reached sooner than with a lower one.

5.4 Sinusoidal Profile

A sinusoidal profile, given by $z = a \sin bx$, with amplitude $2a$ and wavelength $w = 2\pi/b$ (or aspect ratio $2a/w$), is plotted in Fig. 28. D_{R1} for this profile is given by:

$$D_{R1} = \sqrt{2/3}\left[\tan^{-1}(2\pi a/w)\right]^{3/2}. \tag{18}$$

which shows that the profile roughness increases nonlinearly as the wavelength w decreases or the amplitude 2a increases. It is noted that by comparing equations 18 and 15, a sinusoidal profile is found to exhibit a larger range of roughness values than a symmetric triangular profile. This is because the maximum deviation of the unit normal vectors to a sinusoidal profile is larger than that of a symmetric triangular profile of equivalent aspect ratio.

A constant asperity wavelength was assumed, so that by increasing the asperity amplitude the effect of the fracture roughness could be investigated. Different values of $2a/w$ were studied under the normal stress set equal to 1.0, 3.0,

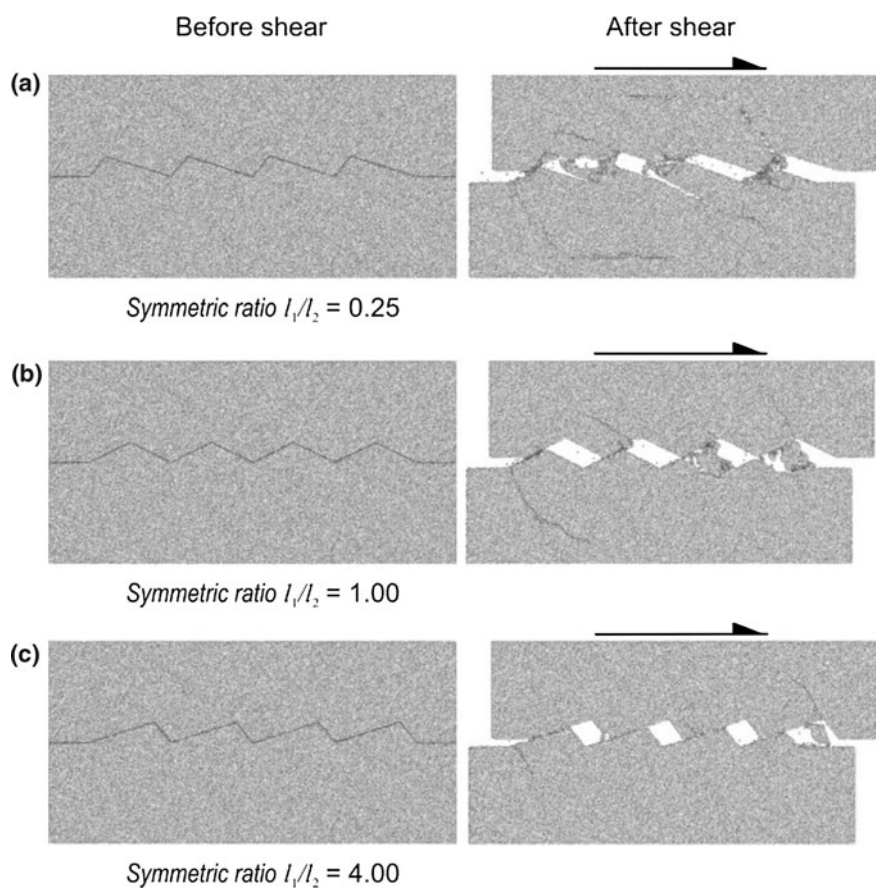

Fig. 26 Effects of asperity symmetry ratio on profile shear strength: **a** $l_1/l_2 = 0.25$, **b** $l_1/l_2 = 1.0$ and **c** $l_1/l_2 = 4.0$ under 1.0 MPa normal stress

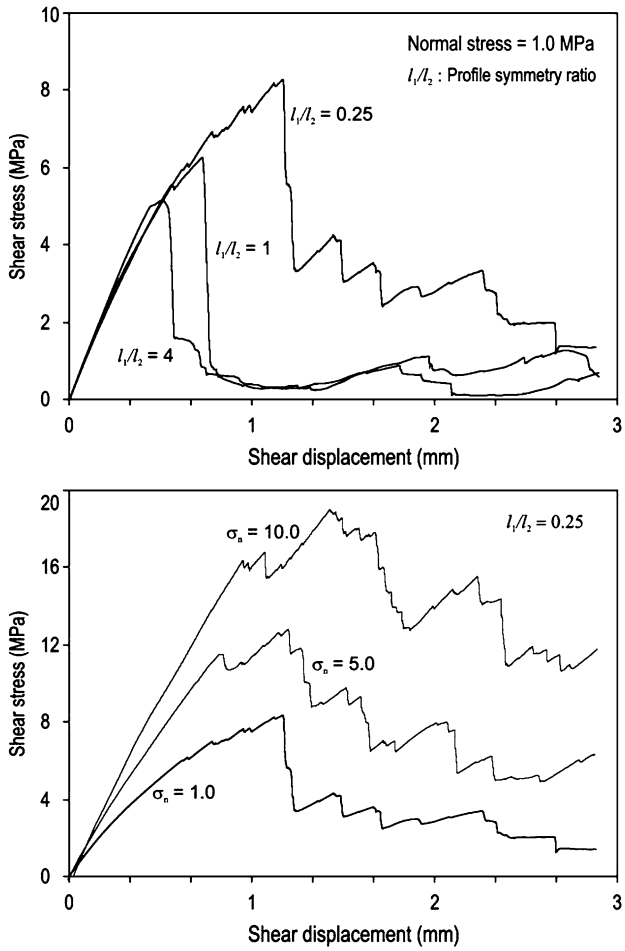

Fig. 27 Shear stress versus shear displacement curves for an asymmetric profile with different symmetry ratios

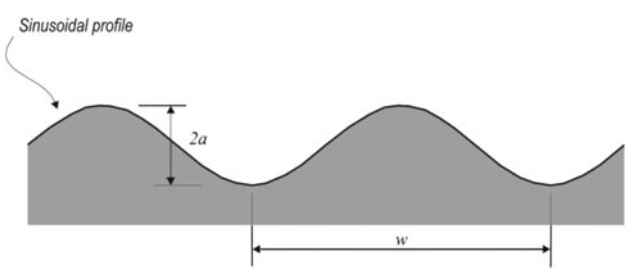

Fig. 28 Geometrical features of a sinusoidal profile (Rasouli 2002)

and 5.0 MPa, respectively. Figure 29 shows the results from shear testing simulations for two values of $2a/w$ and 1.0 MPa normal stress, where also given for comparison purposes are the results for a symmetric triangular profile with identical aspect ratios. It is observed that in general the shear strength increases with the profile aspect ratio increasing. Both shear and tensile cracks develop nearly at the same locations, however the sinusoidal profiles exhibit larger shear strength values and more damage compared to the triangular profiles. This is likely due to the surface being exposed to shearing being larger for a sinusoidal profile than a triangular one.

A comparison of the shear strength of synthetic triangular profiles with 30° asperity angle (dashed line) with the corresponding sinusoidal profile with $2a/w$ = 0.288 (solid line) is illustrated in Fig. 30a. A considerable difference between the peak shear strength values is observed, which is likely due to the effect of the shape of the asperities. In addition, the residual shear strength is shown to change from about 0.5 MPa for a triangular profile to approximately 3.0 MPa for a sinusoidal profile. The shear stress versus shear displacement curves obtained for the sinusoidal profile with $2a/w$ = 0.288 under the normal stress in the range 1.0–10.0 MPa are plotted in Fig. 30b. It is shown that the shearing behaviour of the sinusoidal profiles is fairly similar to the corresponding triangular profiles, the only difference being that the former fractures exhibit slightly larger peak and residual shear strength values.

Table 4 gives D_{R1} for the simulated profiles together with the corresponding peak and residual shear strength values. It is seen that the strength as well as the corresponding D_{R1} values are larger for sinusoidal profiles. This demonstrates that the presence of sharp asperities along a fracture profile is to reduce the peak and residual shear strengths significantly. This can also be applied to hammered and corrugated fractures where a hammered fracture is less prone to have spiky and sharp asperities than a corrugated one. The results obtained from the PFC2D simulations confirm that the sinusoidal profiles show a larger range of roughness values than the corresponding symmetric triangular profiles. This conclusion agrees well with the results reported by Rasouli and Harrison (2010) through multivariate analyses of profile roughness.

5.5 Randomly Generated Profiles

To assess the applicability of D_{R1} to the estimate of the shear strength of fractures with more complex geometries, profiles were generated using a simple linear random generation algorithm. The width of each profile is 10 cm and the amplitude of the asperities is taken to vary between 0.0 and 0.5 cm. The generated profiles (named A to J) are shown in Fig. 31 with the corresponding D_{R1} value.

In general, D_{R1} is estimated from the statistical analysis of the normal unit vectors corresponding to a rock fracture profile extracted at a given scale. Figure 31 shows that profiles A to E consist of 10 asperities, whereas profiles F to J consist of 5 asperities. The symmetry ratio l_1/l_2 for all the profiles is assumed to be equal to 3, which allows one to study the fracture shear strength directionality.

The D_{R1} values of the profiles with 10 asperities (A to E) are expected to be greater than those with 5 asperities

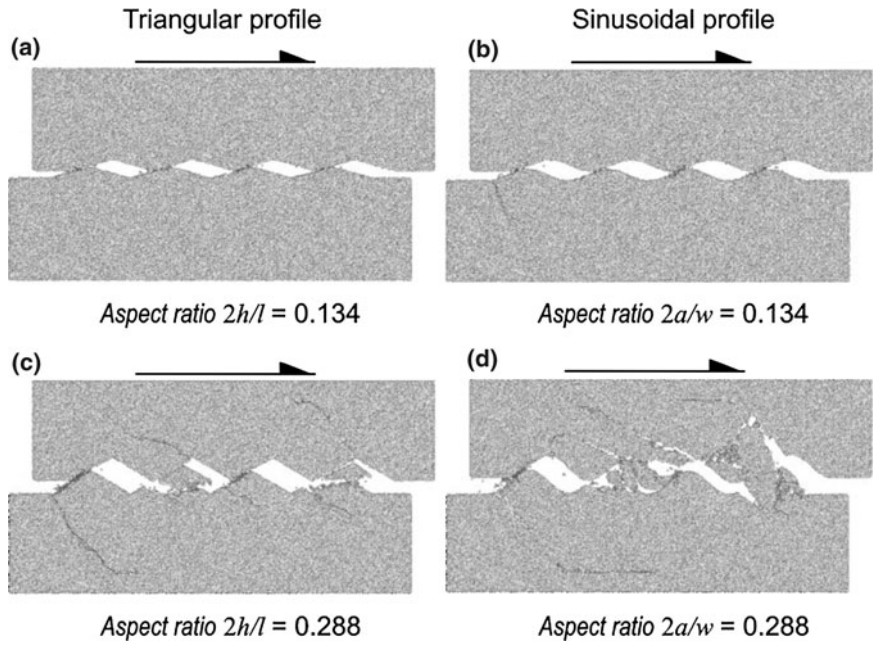

Fig. 29 Comparison between shearing response of a synthetic triangular (**a** and **c**) and a sinusoidal (**b** and **d**) profiles under 1.0 MPa normal stress

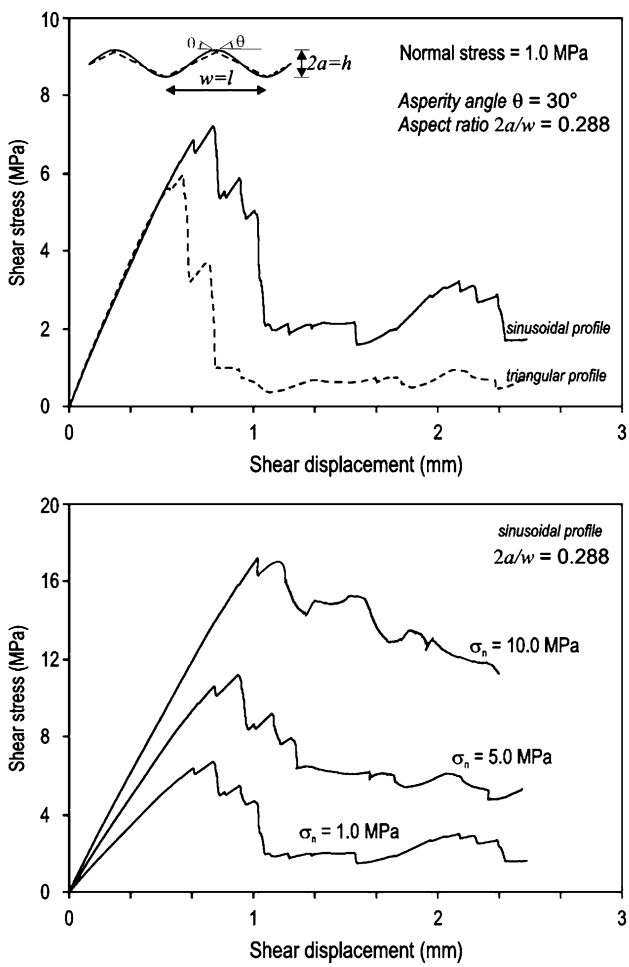

Fig. 30 Comparison between shear strength of synthetic triangular (**a** and **c** in Fig. 29) and sinusoidal (**b** and **d** in Fig. 29) profiles under 1.0 MPa normal stress

Table 4 Comparison of roughness and shear strength of a triangular and sinusoidal profile

Fracture ID	Property	Peak shear stress (MPa)	Residual shear stress (MPa)	D_{R1}
Triangular profile	$\theta = 30°$, $2h/l = 0.288$	6.0	0.45	0.280
Sinusoidal profile	$2a/w = 0.288$	7.3	2.10	0.515

(profiles F to J). This is due to the larger asperity wavelengths for profiles F to J which results in asperity base angles smaller than those for profiles A to E. Accordingly, assuming that a correlation exists between profile roughness and shear strength, the shear strengths of profiles A to E are expected to be greater than those of profiles F to J.

PFC2D shear test simulations were performed by shearing in opposite directions so as to investigate the fracture strength directional dependency. Three different normal stresses of 1, 5, and 10 MPa were used to capture different failure mechanisms. Figure 32 shows the profiles A to E after shearing at 1.0 MPa normal stress. The profiles on the left correspond to left to right shearing, whereas those on the right are for shearing from right to left. In both cases, the upper block moves with a constant shear rate as the lower one is fixed.

In shearing profiles A and C form left to right, the profile C with less harsh asperities in the direction of shearing exhibits a smaller shear resistance than profile A. It is noted that a 1.0 MPa normal stress is not large enough to develop tensile cracks through the intact sample. It is also observed that significant differences are

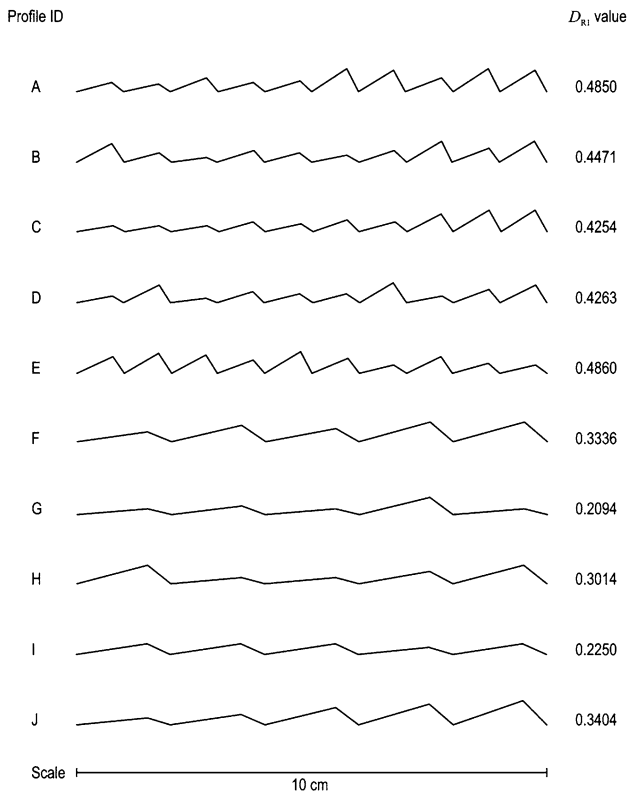

Fig. 31 Randomly generated profiles with different D_{R1} values. Profile's projected length is 10 cm

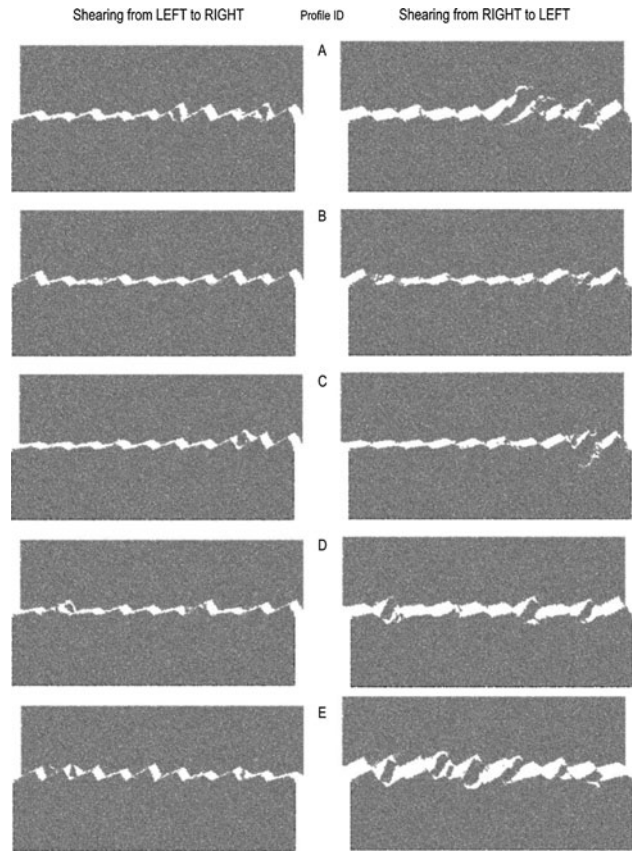

Fig. 32 View of sheared samples (profiles **a** to **e**) in PFC2D fracture shear test box under 1.0 MPa normal stress

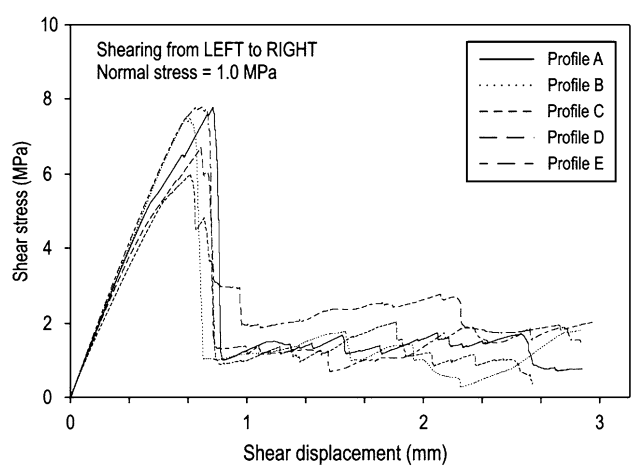

Fig. 33 Shear stress versus shear displacement curves for profiles *A* to *E* simulated at 1.0 MPa normal stress: shearing from left to right

obtained by shearing in two different directions, which again illustrates the directional dependency of the fracture. Shear strength is greater when shearing the fracture from right to left, as expected.

As noted, every single asperity along the profile has the symmetry ratio l_1/l_2 equal to 3 which causes a severe shear strength dependence on the shearing direction. This can be quantified by measuring the average mean angle of the left and right chords (θ^+ and θ^-) of each asperity. Furthermore, asperity damage is observed in profiles A and C, when the fractures are sheared from right to left. Asperity cut-off is also observed in profiles D and E where the high angle asperities are located against the shearing direction.

Figure 33 shows the shear stress versus shear displacement curves for profiles A to E and for shearing from left to right. Similar results for shearing in the opposite direction are given in Fig. 34. It is observed, based on the shear strength values, that these factures are sheared more easily from left to right than from right to left. In addition, the fracture profiles A to E with higher asperity amplitudes, when sheared from left to right, exhibit larger residual shear strength values. In addition, when profile E is sheared from right to left it exhibits a larger peak and smaller residual shear strengths in comparison with other profiles.

Figure 35 shows the fractures with profiles F to J after shearing under 1.0 MPa normal stress, with the specimens sheared from left to right in the right column. Shearing in both directions results in the upper block moving with a constant shearing rate over the lower one which is kept fixed. The most significant difference between the shearing response of profiles A to E and that of profiles F to J is the effect of the number of asperities along each profile (i.e. 10

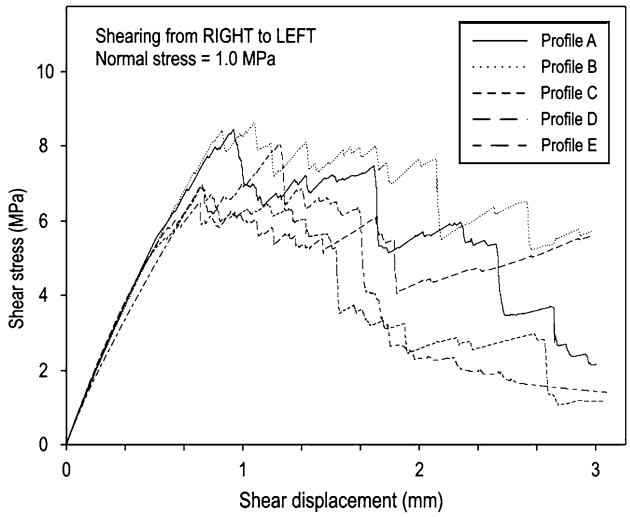

Fig. 34 Shear stress versus shear displacement curves for profiles *A* to *E* simulated at 1.0 MPa normal stress: shearing from right to left

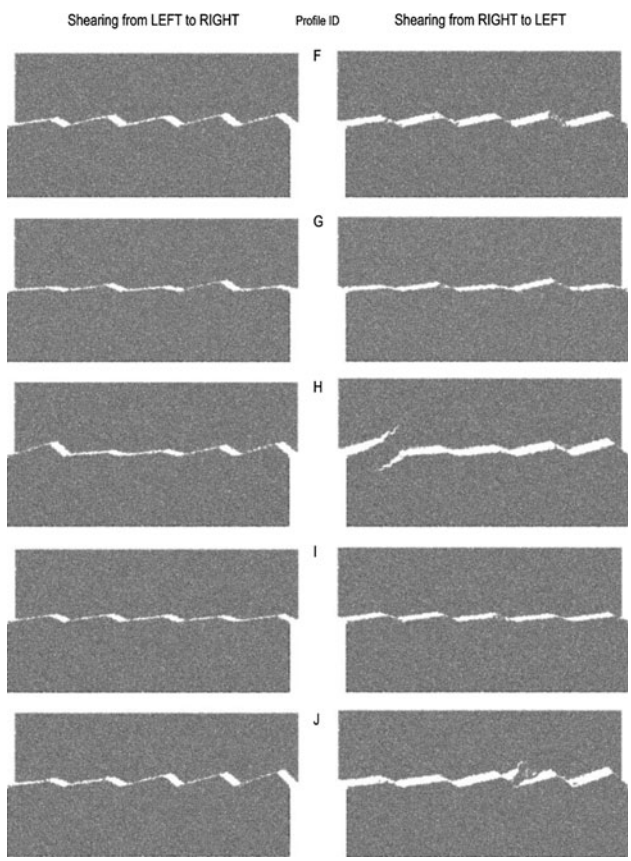

Fig. 35 View of sheared samples (profiles **f** to **j**) in PFC2D fracture shear test box under 1.0 MPa normal stress

for profiles A to E and 5 for profiles F to J). It is observed that a smaller number of asperity breakage and cut-off occurs, which is apparently due to the decrease in the

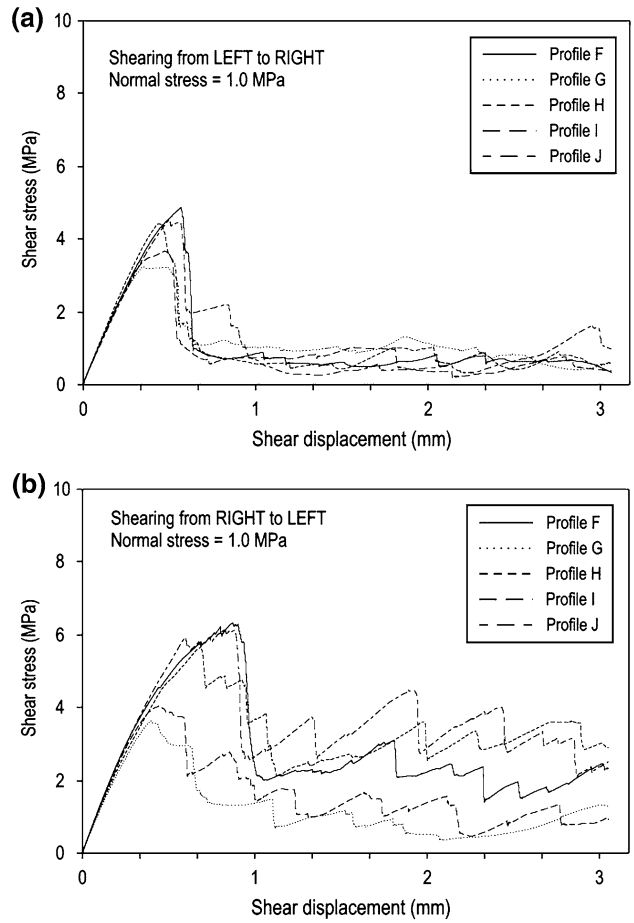

Fig. 36 Shear stress versus shear displacement curves for profiles *F* to *J* simulated at 1.0 MPa normal stress: shearing from left to right

number of asperities which may result in smaller surface roughness and shear strength. Generally, the magnitude and extent of asperity damage in profiles F to J are much less than what is observed for profiles A to E.

Figure 36 shows the curves of shear stress versus shear displacement for fracture profiles F to J when they are sheared left to right (Fig. 36a) and right to left (Fig. 36b), respectively. It is seen that the peak shear strength is smaller compared to that of profiles A to E. Given the difference in the number of asperities (5 in profiles F to J and 10 in profiles A to E), with the profile roughness increasing as the asperity wavelength decreases (or say the asperity amplitude increasing), larger wavelengths result in a more flat and planar profile, which in turn reduces the shear strength.

Comparing the shear stress versus shear displacement curves of all the profiles from A to J when sheared from right to left, the residual shear strength of the profiles with 10 asperities (A to E) is much greater than that of the profiles with 5 asperities (F to J). The same comparison of the curves of the profiles A to E does not exhibit a large

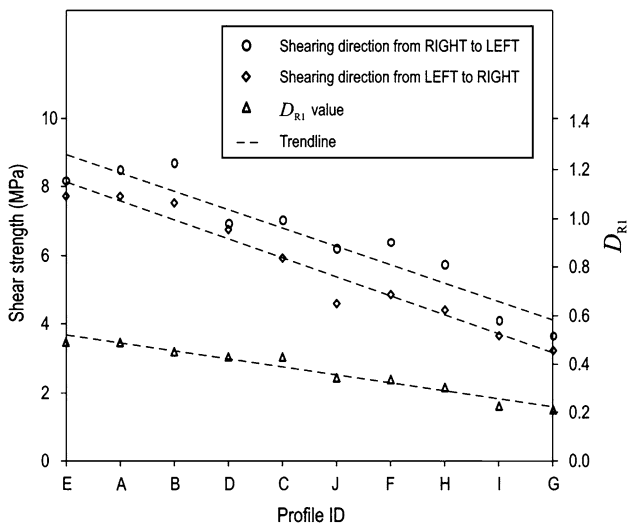

Fig. 37 Shear strength of profiles *A* to *J* in both directions together with profiles' D_{R1} values

reduction from the peak to the residual strength values, although this is more significant for profiles F to J. This difference is most likely a result of the first set of profiles having larger number of asperities.

Figure 37 shows the peak shear strength values of profiles A to J obtained from PFC2D simulations by shearing in both directions (from left to right and from right to left). The peak shear strengths are ordered according to the corresponding D_{R1} value (D_{R1} is shown on the right axis of the plot). Independent of the small fluctuations shown, the general trend is for the peak strength of randomly generated profiles sheared in both directions to decrease as the D_{R1} decreases. A visual comparison of the profiles given in Fig. 31 verifies that the general trend obtained from the PFC2D simulations and the D_{R1} analyses are in good agreement.

6 Correlations Between D_{R1} and Peak Shear Strength

It is of interest to analyse the possible correlations between D_{R1} and the peak shear strength of fractures having symmetric triangular profiles. To express the shear strength in terms of the profile asperity angle a parametric cubic spline curve is used. In numerical analysis, cubic spline fitting is a form of interpolation where the interpolant is a special type of piecewise polynomial called a spline.

As illustrated in Fig. 38, in a parametric form cubic splines comprise a start point (p_1), an end point (p_2), and a number of control points (here 2 control points cp_1 and cp_2 are introduced) which lie between the start point with coordinates (x_1, y_1) and the end point with coordinates(x_2, y_2). Between these points the spline curves may be written as (Piegl and Tiller 1997):

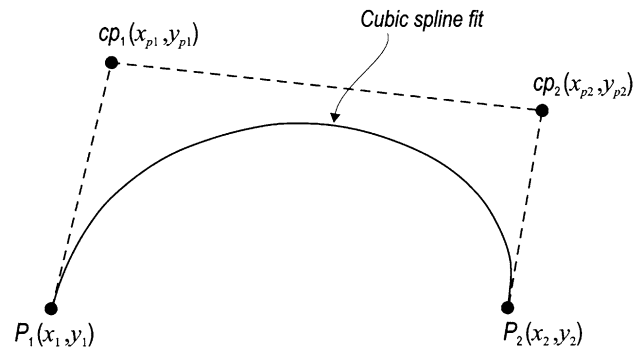

Fig. 38 Schematic of parametric cubic spline with four points

$$\begin{aligned} X &= Ax_1 + Bx_{p1} + Cx_{p2} + t^3 x_2 \\ Y &= Ay_1 + By_{p1} + Cy_{p2} + t^3 y_2 \end{aligned} \tag{19}$$

where (x_{p1}, y_{p1}) and (x_{p2}, y_{p2}) are the coordinates of the two control points that determine the shape of the spline curve and the coefficients *A*, *B* and *C* are given by:

$$\begin{aligned} A &= -t^3 + 3t^2 - 3t + 1,\ B = 3t^3 - 63t^2 + 3t,\ C \\ &= -3t^3 + 3t^2 \end{aligned} \tag{20}$$

with $0 \le t \le 1$.

A plot of the peak shear strength versus the normal stress, for symmetric triangular profiles with asperity angles of 15°, 30°, and 45°, was given in Sect. 5.2 based on the PFC2D simulation results. The normal stresses corresponding to the point $\sigma_n|_{\alpha=0}$ where the fracture shear strength envelopes intersect the intact rock material curve, for the three mentioned synthetic profiles, were calculated analytically and verified by numerical simulations (Table 3). $\sigma_n|_{\alpha=0}$ is used as the end point of cubic splines.

In the following, parametric cubic splines are to be fitted to the data plotted in Fig. 22 based on the following assumptions:

- The fracture is assumed to have no cohesion and hence the start point is at the origin, i.e. $(x_1, y_1) = (0, 0)$.
- The end point (x_2, y_2) is where the shear strength envelope meets the intact rock envelope; it is determined using Eq. 14 and the peak strength criterion of the intact rock $\tau = c + \sigma_n \tan\varphi$ as:

$$(x_2, y_2) = \left(c(\cot D_{R1} - \tan\varphi)\cos^2\varphi,\ c\left(\cos^2\varphi + \frac{\sin 2\varphi}{2\tan D_{R1}}\right)\right). \tag{21}$$

- The tangent vector at the origin is vertical, so that the first control point takes the general form $(x_{p1}, y_{p1}) = (0, y_{p1})$.

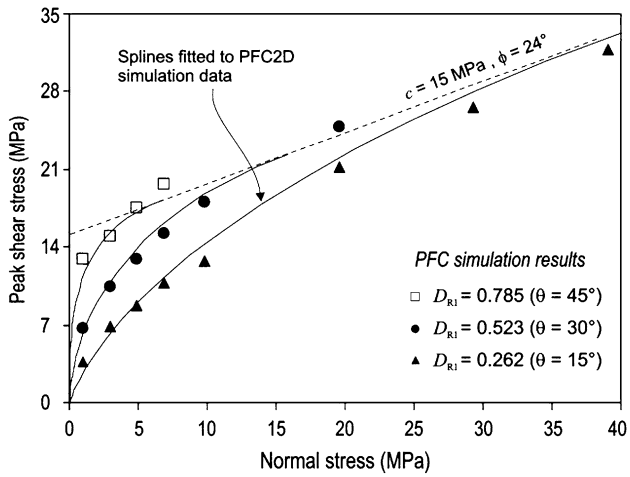

Fig. 39 Cubic splines fitted to the shear strength data of symmetric triangular profiles obtained from PFC2D simulations

- The second control point is$(x_2, y_2) = (0, y_{p2})$, where the value of y_{p2} is equivalent to the cohesion (c) of the intact rock. This ensures that all the curves are tangent to the intact rock envelope at the intersection point.

These assumptions show that the only variable controlling the fit of the cubic spline to the results of the numerical analysis is the position of the first control point, i.e. y_{p1}. The mechanical properties of the rock (cohesion and friction angle, c and ϕ) and the roughness angle (θ, which is D_{R1} for a symmetric triangular profile) are other factors considered in the calculations. For any particular value of D_{R1}, it is straightforward to identify the value of y_{p1} that gives the best fit spline to the numerical analysis output.

The results of this are given in Fig. 39 which shows that the cubic splines fit the data quite well. The values of y_{p1} corresponding to the D_{R1} values of 0.262, 0.523 and 0.785 are −2, 1 and 8, respectively. These results lead to the relation:

$$y_{p1} = 29.18D_{\mathrm{R1}}^2 - 11.46D_{\mathrm{R1}} - 1, \tag{22}$$

which has a coefficient of determination close to unity.

The assumptions listed above together with Eq. 22 allow one to write Eq. 19 as follows:

$$\begin{aligned}\sigma_{\mathrm{n}} &= ct^3(\cot D_{\mathrm{R1}} - \tan\varphi)\cos^2\varphi \\ \tau &= \left(3t^3 - 6t^2 + 3t\right)\left(29.18D_{\mathrm{R1}}^2 - 11.46D_{\mathrm{R1}} - 1\right) \\ &\quad + 3ct^2(1-t) + ct^3\left(\cos^2\varphi + \frac{\sin 2\varphi}{2\tan D_{\mathrm{R1}}}\right)\end{aligned} \tag{23}$$

which give the estimated shear strength value to be used for other profile asperity angles. This procedure will be used in the following section to estimate the shear strength of rock fracture profiles.

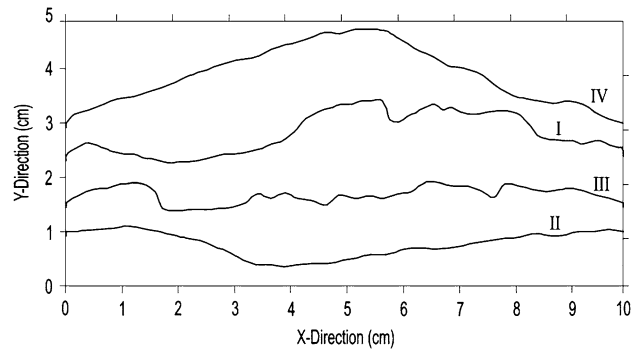

Fig. 40 Geometry of rock fracture profiles (*I* to *IV*) after Rasouli and Harrison (2010)

7 Analysis of Rock Fracture Profiles

The shear behaviour of several rock fracture profiles was finally analysed by using the results of PFC2D shear test simulations with the aim to investigate the possible correlation between D_{R1} and the shear strength. Four rock fracture profiles (profiles I to IV as given by Rasouli 2002) with the geometries shown in Fig. 40 were used. The D_{R1} values for these profiles estimated numerically at a sampling size close to zero are 0.3612, 0.1911, 0.3404 and 0.3543 for profiles I to IV, respectively. According to these D_{R1} values profile I is expected to be the roughest with the highest shear strength and profile II the smoothest with the lowest shear strength. Similar shear strength values are expected for profiles I and IV again based on the D_{R1} values.

The fracture with profiles I to IV were modelled with PFC2D in a shear box with the same micro-properties as applied to the synthetic profiles. Figure 41 shows these fractures after shearing at 3.0 MPa normal stress. Interestingly, D_{R1} shows an increasing trend with the increase of the shear strength, anticipating a possible correlation between D_{R1} and the shear strength for real rock fractures. Figure 42 shows the peak shear stress versus shear displacement curves for the same fracture profiles I to IV. The peak shear strength is observed to increase with the increase of D_{R1}. This same increasing trend is not evidenced for the residual shear strength, which is likely due to the significant differences between waviness (or say bumpiness) and roughness of the fractures being considered.

The shear strength of the same fractures was also estimated for different normal stress values. Figure 43 shows that the shear strength increases with the increase of both D_{R1} and normal stress. As for the synthetic profiles, cubic splines were fitted to the simulation data. To determine the end points of the cubic splines a simplified approach based on the analytical solutions developed for the symmetric triangular profiles was used.

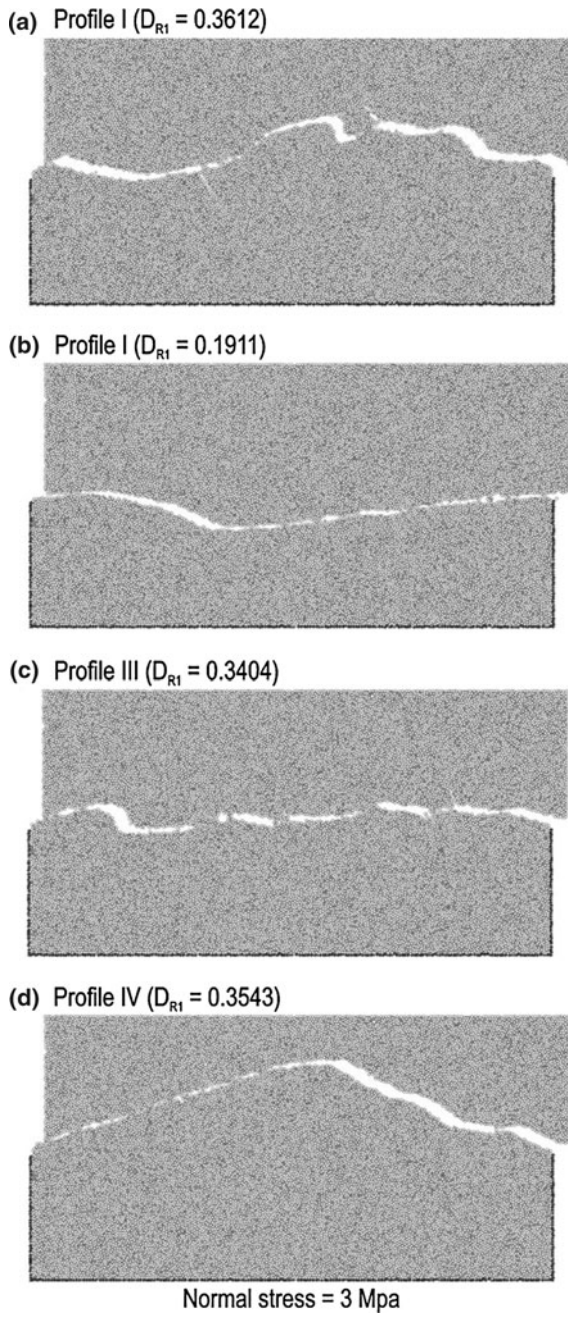

Fig. 41 Visual comparison of shearing progress of rock fracture profiles (*I* to *IV*) with different roughness (D_{R1}) at 3.0 MPa normal stress modelled in PFC2D

The base angle θ of a symmetric triangular profile corresponding to the D_{R1} value of each fracture profile was calculated and Eq. 14 was used to determine the end point of the splines. The values of y_{p1} corresponding to D_{R1} values of 0.1911, 0.3404 and 0.3612 are −3, 0 and 7, respectively. These results lead to:

$$y_{p1} = e^{(57.94D_{R1}-18.624)} - 3.008. \tag{24}$$

By substituting this in Eq. 19, the shear strength curve corresponding to rock fracture profiles having different

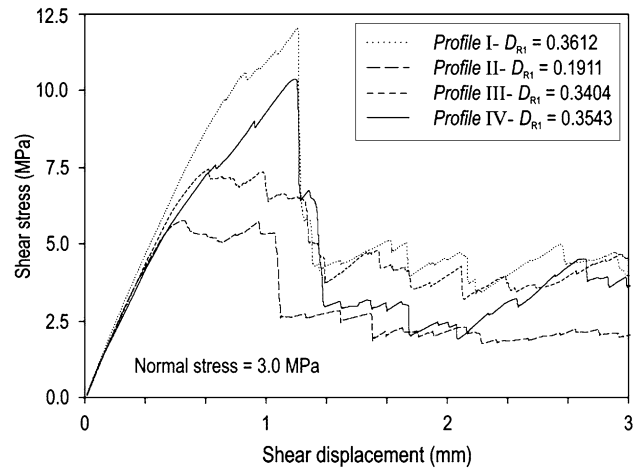

Fig. 42 PFC2D simulation of rock fracture profiles (*I* to *IV*) with different roughness (D_{R1}) at a 3 MPa normal stress

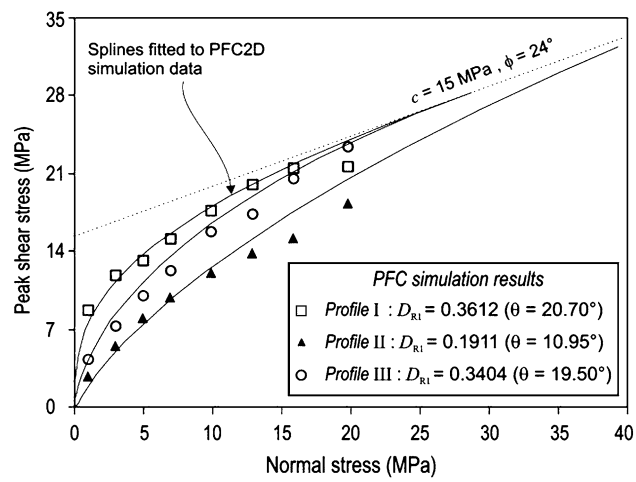

Fig. 43 Cubic splines fitted to shear strength data of rock fracture profiles

D_{R1} values is obtained. With the same procedure adopted for symmetric profiles and by using Eqs. 19, 21, and 24, the shear strength curve corresponding to a fracture with given roughness parameter D_{R1} and intact rock properties c and ϕ for a range of normal stress values can be estimated as:

$$\sigma_n = ct^3(\cot D_{R1} - \tan\varphi)\cos^2\varphi$$
$$\tau = \left(3t^3 - 6t^2 + 3t\right)\left(e^{(57.94D_{R1}-18.624)} - 3.008\right) + 3ct^2(1-t) + ct^3\left(\cos^2\varphi + \frac{\sin 2\varphi}{2\tan D_{R1}}\right). \tag{25}$$

which are similar to Eq. 23 obtained for synthetic profiles. The only difference is in the control point 1 in which y_{p1} is related to profile D_{R1} based on Eq. 24.

Figure 43 shows the cubic splines obtained by fitting Eq. 25 to the peak shear strength values given by PFC2D simulations. The analyses show that the fracture peak

shear strength data are well fitted by cubic splines which in turn give good estimates of the shear strength. Although the applicability of this correlation may be limited at this stage, it is clearly shown that D_{R1} is a representative parameter which characterises the profile roughness and could be employed in shear strength estimation of rock fractures.

8 Conclusions

In the first part of this paper the bonded particle model (BPM) implemented in the particle flow code (PFC) (Itasca Consulting Group 2008) is discussed and typical limitations of 2D versus 3D modelling of rock-like materials are highlighted. Then, the results of the sensitivity analyses performed by using the two-dimensional particle flow code (PFC2D) are presented to show how the micro-properties of the model are relevant to obtain the corresponding macro-response.

The influence of the most significant micro-properties in PFC2D modelling, including particle size, contact elasticity, ratio of contact normal to shear stiffness, and bond strength are analysed by simulation of unconfined and confined biaxial tests. The uniaxial compressive strength (UCS) and Young's modulus (E) of rock-like materials are determined based on the correlations developed for different scenarios. A set of micro-properties for a weak rock with UCS approximately equal to 42 MPa is then defined as applied to shear test simulations.

The PFC2D scheme adopted for shear test simulations is discussed in detail. The effects of bonding type, micro-roughness (i.e. distribution of particles along the fracture), and fracture particles friction coefficient on the fracture shear strength are investigated by shear test simulations of synthetic fracture profiles. The fracture particle friction coefficient is calibrated for both smooth and rough fractures and the sensitivity of shear strength to this micro-parameter is discussed, to finally select a low value (0.05) for simulation purpose. The influence of the intact material bond strength on asperity degradation during shearing is analysed in detail. It is shown that PFC2D is capable of tracing the development of micro-cracks during fracture shearing for different normal stress levels.

Synthetic and rock fracture profiles are then simulated during direct shear tests with PFC2D. The effects of profile roughness, shearing direction, and normal stress on fracture shear strength and asperity degradation are investigated. During fracture shearing, the evolution of asperity degradation is visually and quantitatively presented and discussed based on the observed failure patterns. The directional dependency of the fracture shear strength is highlighted with the simulation of randomly generated profiles. Peak and residual shear strength values and failure modes of the simulated fractures are shown to well represent the results obtained in laboratory tests and by analytical solutions. The feasibility of reproducing a fracture and estimating its mechanical behaviour using BPM is assessed.

The roughness parameter D_{R1} for synthetic and for four representative rock fracture profiles is finally applied to find that in most cases the values of the peak shear strength as estimated with the PFC2D simulations are well correlated. Also D_{R1} is found to be representative of the peak shear strength values estimated and the parametric cubic splines are shown to well fit the data obtained from PFC2D simulations. Finally, correlations are developed to estimate the shear strength of both symmetric triangular and rock fracture profiles.

References

Asadi MS (2011) Experimental and PFC2D numerical study of progressive shear behaviour of single rough rock fractures. PhD Thesis, Curtin University, Perth

Asadi MS, Rasouli V (2010) Direct shear test simulation of real rough rock fractures, Eurock2010. Luasanne, Zwitzerland

Asadi MS, Rasouli V (2011) PFC2D simulation of directionality in rough fractures shear strength. In: 2nd International FLAC/DEM Symposium, Ist edn. Itasca Consulting Group, Melbourne

Asadollahi P, Tonon F (2010) Degradation of rock fracture asperities in unloading, reloading, and reversal. Int J Numer Anal Methods Geomech 35(12):1334–13046

Bandis SC, Lumsden AC, Barton NR (1983) Fundamentals of rock joint deformation. Int J Rock Mech Min Sci Geomech Abstracts 20:249–268

Barton N (1973) Review of a new shear-strength criterion for rock joints. Eng Geol 7:287–332

Barton N, Choubey V (1977) The shear strength of rock joints in theory and practice. Rock Mech Rock Eng 10:1–54

Belem T, Homand-Etienne F, Souley M (2000) Quantitative parameters for rock joint surface roughness. Rock Mech Rock Eng 33:217–242

Belem T, Souley M, Homand F (2007) Modeling surface roughness degradation of rock joint wall during monotonic and cyclic shearing. Acta Geotech 2:227–248

Bruno MS, Nelson RB (1991) Microstructural analysis of the inelastic behavior of sedimentary rock. Mech Mater 12:95–118

Cho N, Martin CD, Sego DC (2007) A clumped particle model for rock. Int J Rock Mech Min Sci 44:997–1010

Cho N, Martin CD, Sego DC (2008) Development of a shear zone in brittle rock subjected to direct shear. Int J Rock Mech Min Sci 45:1335–1346

Cundall PA (2000) Numerical experiments on rough joints in shear using a bonded particle model. In: Lehner FK, Urai JL (eds) Aspects of tectonic faulting. Springer, Berlin, pp 1–9

Ferrero A, Migliazza M, Tebaldi G (2010) Development of a new experimental apparatus for the study of the mechanical behaviour of a rock discontinuity under monotonic and cyclic loads. Rock Mech Rock Eng 43:685–695

Giacomini A, Buzzi O, Krabbenhoft K (2008) Modeling the asperity degradation of a sheared rock joint using FEM. In: 8th World Congress on Computational Mechanics (WCCM8), Venice, Italy

Huang TH, Chang CS, Chao CY (2002) Experimental and mathematical modeling for fracture of rock joint with regular asperities. Eng Fract Mech 69:1977–1996

ISRM (1978) International society for rock mechanics commission on standardization of laboratory and field tests: suggested methods for the quantitative description of discontinuities in rock masses. Int J Rock Mech Min Sci Geomechan Abstracts 15:319–368

Itasca Consulting Group I (2008) PFC2D-particle flow code in two dimensions. Itasca Consulting Group I, Minnesota

Ivars DM, Potyondy DO, Pierce M, Cundall PA (2008) The smooth-joint contact model. In: 8th World Congress on Computational Mechanics (WCCM8); 5th European congress on computational methods in applied sciences and engineering (ECCOMAS 2008), Venice, Italy

Jing L, Stephansson O (2007) Fundamentals of discrete element methods for rock engineering: theory and applications. Elsevier, Amsterdam

Karami A, Stead D (2008) Asperity degradation and damage in the direct shear test: a hybrid FEM/DEM approach. Rock Mech Rock Eng 41:229–266

Koyama T, Jing L (2007) Effects of model scale and particle size on micro-mechanical properties and failure processes of rocks–A particle mechanics approach. Eng Anal Boundary Elem 31:458–472

Lambert C, Buzzi O, Giacomini A (2010) Influence of calcium leaching on the mechanical behavior of a rock-mortar interface. A DEM Anal Comput Geotech 37:258–266

Lee HS, Park YJ, Cho TF, You KH (2001) Influence of asperity degradation on the mechanical behavior of rough rock joints under cyclic shear loading. Int J Rock Mech Min Sci 38:967–980

Park J-W, Song J-J (2009) Numerical simulation of a direct shear test on a rock joint using a bonded-particle model. Int J Rock Mech Min Sci 46:1315–1328

Patton F (1966) Multiple modes of shear failure in rock. In: Proceedings of the 1st international congress on rock mechanics, vol 1. Lisbon, pp 509–13

Piegl L, Tiller W (1997) The NURBS Book. Springer-Verlag, Berlin¸ Heidelberg

Plesha ME (1987) Eigenvalue estimation for dynamic contact problems. J Eng Mech 113:457–462

Potyondy DO, Cundall PA (2004) A bonded-particle model for rock. Int J Rock Mech Min Sci Geomech Abstracts 41:1329

Rasouli V (2002) Application of Riemannian multivariate statistics to the analysis of rock fracture surface roughness. Imperial College of Science, Technology and Medicine, London

Rasouli V, Harrison JP (2010) Assessment of rock fracture surface roughness using Riemannian statistics of linear profiles. Int J Rock Mech Min Sci 47:940–948

Saito H, Grasselli G, Ferrero A (2007) Accounting for local roughness in geostatistical simulation of fracture surface topography. Rock mechanics: meeting society's challenges and demands. Taylor & Francis, Boca Raton, pp 167–175

Wang C, Tannant DD, Lilly PA (2003) Numerical analysis of the stability of heavily jointed rock slopes using PFC2D. Int J Rock Mech Min Sci 40:415–424

Yang ZY, Chiang DY (2000) An experimental study on the progressive shear behavior of rock joints with tooth-shaped asperities. Int J Rock Mech Min Sci 37:1247–1259

Yoon J (2007) Application of experimental design and optimization to PFC model calibration in uniaxial compression simulation. Int J Rock Mech Min Sci 44:871–889